J. Fluid Mech. (2008), *vol.* 609, *pp.* 377–410.
doi:10.1017/S0022112008002516 Printed in the United Kingdom

Buoyancy-driven motion of a gas bubble through viscous liquid in a round tube

JAMES Q. FENG

Cardiovascular R & D, Boston Scientific Corporation, Three Scimed Place C-150, Maple Grove, MN 55311, USA
james.feng@bsci.com

(Received 7 January 2008 and in revised form 10 May 2008)

The steady axisymmetric flow of viscous liquid relative to a gas bubble due to its buoyancy-driven motion in a round tube is computed by solving the nonlinear Navier–Stokes equations using a Galerkin finite-element method with a boundary-fitted mesh. When the bubble is relatively small compared with the tube size (e.g. the volume-equivalent radius of the bubble is less than a quarter of the tube radius R), the bubble exhibits similar behaviour to one moving in an extended liquid, developing a spherical-cap shape with increasing Reynolds number (Re) if the capillary number is not too small. The long-bubble (also known as a Taylor bubble) characteristics can be observed with bubbles of volume-equivalent radius greater than the tube radius, especially when the surface tension effect is relatively weak (e.g. for Weber number We greater than unity). The computed values of Froude number Fr for most cases agree well with the correlation formulae derived from experimental data for long bubbles, and even with (short) bubbles of volume-equivalent radius three-quarters of the tube radius. All of the computed surface profiles of long bubbles exhibit a prolate-like nose shape, yet various tail shapes can be obtained by adjusting the parameter values of Re and We. At large Weber number (e.g. $We = 10$), the bubble tail forms a concave profile with a gas 'cup' developed at small Re and a 'skirt' at large Re with sharply curved rims. For $We \leqslant 1$, the bubble tail profile appears rounded without large local curvatures, although a slightly concave tail may develop at large Re. non-uniform annular film adjacent to the tube wall is commonly observed when Weber number is small, especially for bubbles of volume $<3\pi R^3$, suggesting that the surface tension effect can play a complicated role. Nonetheless the computed value of Fr is found to be generally independent of the bubble length for bubbles of volume-equivalent radius greater than the tube radius. If the bubble length reaches about 2.5 tube radii, the value of its frontal radius becomes basically the same as that for long bubbles of much larger volume. An examination of the distribution of the z-component of traction along the bubble surface reveals the basic mechanism for long bubbles rising at a terminal velocity that is independent of bubble volume.

1. Introduction

A gas bubble moving through liquid in a round tube can exhibit various behaviours of both theoretical and practical interest. The liquid flow as well as the deformable bubble shape are expected to be axisymmetric, when the centre of volume of the bubble remains on the centreline of the tube along which the driving force (such as buoyancy) is directed. The motion of the bubble relative to the tube wall can either be

driven by a buoyancy force, as in a vertical tube in an earthbound environment, or be pushed by a liquid flow due to an externally applied pressure gradient, or both. If the driving mechanism (such as the buoyancy force) is time-independent, the consequent bubble motion is expected to be steady, except at relatively large values of Reynolds number when an unsteady or even turbulent wake develops. For convenience of rigorous analysis, the present work is restricted to the case of buoyancy-driven bubble motion with a steady axisymmetric laminar flow field.

For bubbles in large tubes with negligible or weak wall effect, the buoyancy-driven terminal velocity of bubble motion increases with the bubble volume, as expected based on a balance of buoyant weight and drag. Smaller bubbles moving at lower terminal velocities exhibit nearly spherical shape due to the relatively strong surface tension effect. With increasing the bubble size, the terminal velocity increases and the bubble shape becomes more oblate. Large bubbles moving in extended liquids (with container walls far away) have been often found to take an apparently steady 'spherical cap' shape with either laminar or turbulent wakes (cf. Davies & Taylor 1950; Wegener & Parlange 1973; Bhaga & Weber 1981). Owing to the nonlinear nature of the problem, early theoretical studies were limited to cases of very small bubble deformations either at high Reynolds number (Moore 1959, 1965) or at low Reynolds number (Taylor & Acrivos 1964; Brignell 1973). The advent of modern high-speed computers has facilitated numerical computations of the steady-state flow field and bubble shape over a range of Reynolds number and Weber number (e.g. Ryskin & Leal 1984), by solving the Navier–Stokes equations in boundary-fitted orthogonal coordinates with a finite-difference scheme. But numerical solutions of strictly steady axisymmetric Navier–Stokes equations for the experimentally observed spherical-cap bubbles (in extended liquids) at Reynolds number $\geqslant 50$ had not been successfully obtained until the recent finite-element computational work of Feng (2007).

When the tube size becomes small compared to the bubble size, or when the bubble is large enough to fill the tube, the terminal velocity of the bubble is found to be practically independent of the bubble volume if the tube diameter and liquid properties are fixed. A relatively large bubble in a (small) tube is often referred to as a long bubble or Taylor bubble in the literature. Long bubbles moving in round tubes typically take a bullet shape with rounded nose (cf. Davies & Taylor 1950; Wallis 1969; Viana *et al.* 2003). According to a recent literature review of Viana *et al.* (2003), the study of long bubbles in tubes dates back to the work of Gibson (1913). Later, prediction formulae for the (buoyancy-driven) terminal velocity of a long bubble in a round tube were derived by many authors such as Dumitrescu (1943), Davies & Taylor (1950), Brown (1965), White & Beardmore (1962), Zukoski (1966), Wallis (1969). Based on a large amount of experimental data for the terminal velocity of buoyancy-driven long-bubble motion in vertical round tubes, Viana *et al.* (2003) presented a set of universal correlation formulae covering large ranges of the buoyancy Reynolds number and Eötvös number. Noteworthy in all those formulae is that the normalized long-bubble terminal velocity, namely the Froude number, is independent of the bubble volume (in contrast to the situation of buoyancy-driven bubble motion in an extended liquid). Thus with a consideration of force balance (of buoyant weight and drag) for long bubbles in tubes, the drag must be nearly proportional to the long-bubble volume because the buoyant weight is determined by the bubble volume.

It is remarkable that the terminal velocity for both spherical-cap bubbles rising in an extended liquid and long bubbles rising in round tubes could be quite accurately predicted by a potential flow analysis considering only the front part of the bubble (namely the bubble nose) based on a given (arc-of-a-circle) shape of the local interface

(see Dumitrescue 1943; Davies & Taylor 1950; Brown 1965; Collins 1965, 1966). A more recent theory of viscous potential flow by Joseph (2003) extended the previous inviscid potential flow models to include viscosity and surface tension effects, leading to predictions of the drag coefficient of spherical-cap bubbles even for Reynolds number less than 50, in good agreement with the empirical formula of Bhaga & Weber (1981) and that obtained by numerically solving the full Navier–Stokes equations (Feng 2007). Funada *et al.* (2005) also applied the theory of viscous potential flow to derive formulae relating the terminal velocity of long bubbles rising in round tubes to Reynolds number, Eötvös number, and aspect ratio of the assumed ellipsoidal shape for the bubble nose, to successfully describe extensive experimental data. However, the potential flow theory is valid when the flow is irrotational, which may be a reasonable approximation for the front part of bubble surface where the boundary layer can remain thin (when Reynolds number is not small and surface curvature is not large as discused by Batchelor 1967). But the potential flow theory cannot describe the separated flow in the wake of the bubble, nor can it be used to accurately model the flow in the thin annular liquid film along the tube wall for analysis of drainage associated with the buoyancy-driven motion of long bubbles in tubes. Hence, a more complete theory is desirable to improve understanding of behaviours of long bubbles in tubes, which often requires numerical solutions of full Navier–Stokes equations.

The problem of viscous flow around a long buoyancy-driven rising bubble in a round tube has been computed numerically by several authors. For example, Reinelt (1987) used a finite-difference method to numerically determine the surface shape and velocity of an air finger rising in a round tube at zero Reynolds number, extending the result of Bretherton (1961) to much larger capillary number. Excluding the bubble tail and wake region, Mao & Dukler (1990, 1991) developed a finite-volume method to compute the liquid flow ahead of and around the bubble, with the bubble velocity iteratively adjusted until the bubble nose takes a locally spherical shape. Multiple numerical solutions were shown to exist and a criterion for determining the physically observable solution was suggested. To include the separated flow in the bubble wake for examining periodic slug flow, Clarke & Issa (1997) assumed a prescribed flat bubble tail (base) shape in their finite-volume computations. The volume-of-fluid computations of Tomiyama, Sou & Sakaguichi (1996) and Bugg, Mack & Rezkallah (1998) eliminated assumptions about the bubble shape and terminal velocity; so they could compute results self-consistently for a number of cases (e.g. Tomiyama *et al.* compared with their own experiments at Eötvös number 4.7, 16.9, 37.3 for Morton number 6.6×10^{-6}, 1.5×10^{-4}, 1.5×10^{-3}, 0.0123, with bubbles about twice the tube diameter long, whereas Bugg *et al.* presented cases at Eötvös number 10, 40, 100 for Morton number 10^{-12}, 10^{-2}, 10, with a bubble of a fixed volume $8\pi R^3/3$ where R is the tube radius). Using a commercial CFD software FLUENT, Taha & Cui (2006) extended numerical solutions to transient three-dimensional turbulent flows around long bubbles, among which they also computed a few cases of laminar flow around axisymmetric bubbles with parameters matching the experiments of Campos & Guedes de Carvalho (1988).

In the present work, numerical solutions are computed for cases ranging from spherical-cap bubbles in relatively large tubes (e.g. bubbles of volume $\pi R^3/48$) to long bubbles in relatively small tubes (e.g. bubbles of volume $3\pi R^3$) by increasing the bubble volume relative to a given reference tube size, in a domain enclosing the entire bubble. A method of Galerkin finite elements with full Newton iterations is used for simultaneously solving the steady axisymmetric Navier–Stokes equations together with the elliptic mesh-generation equations for accurately tracking the entire

bubble surface deformations (cf. Christodoulou & Scriven 1992; de Santos 1991). The computational code used here is the same as described in Feng (2007). Following the descripion of mathematical formulation and computational method in § 2, the results presented in § 3 and § 4 are focused on buoyancy-driven bubble motions in relatively large and small (vertical) round tubes, respectively. The general findings are summarized and further discussed in § 5.

2. Mathematical formulation and computational method

For convenience of computation and analysis, the problem of a gas bubble moving through a liquid of constant density ρ, viscosity μ, and surface tension γ in a round tube is described in terms of dimensionless parameters and variables with length measured in units of the tube radius R, velocity $\boldsymbol{v}$ in units of bubble's terminal velocity U, and pressure p in units of $\mu U/R$. Because the density and viscosity of gases are typically orders of magnitude less than those of liquids, the hydrodynamic stresses due to the flow of gas inside the bubble is completely ignored. A reference frame moving with the bubble is adopted here, with the coordinate origin fixed at the centre of mass of the bubble. Then, the axisymmetric laminar liquid flow around the bubble is governed by the steady incompressible Navier–Stokes equation system

$$\frac{1}{2}Re\,\boldsymbol{v}\cdot\nabla\boldsymbol{v}=\nabla\cdot\boldsymbol{T}\quad\text{with}\quad\boldsymbol{T}\equiv-p\boldsymbol{I}+\nabla\boldsymbol{v}+(\nabla\boldsymbol{v})^{T}\tag{2.1}$$

and

$$\nabla\cdot\boldsymbol{v}=0,\tag{2.2}$$

where Re denotes the Reynolds number defined as $2\rho UR/\mu$, $\boldsymbol{I}$ the identity tensor, and superscript 'T' stands for the transpose.

A cylindrical (z, r)-coordinate system is used with the z-axis coinciding with the axis of symmetry (i.e. the centreline of the tube) and pointing in the same direction as the far-field flow velocity (relative to the bubble). Thus, at the bubble free surface S_f conservation of momentum is satisfied by imposing the traction boundary condition†

$$\boldsymbol{n}\cdot\boldsymbol{T}=\frac{1}{Ca}\left[\frac{\mathrm{d}\boldsymbol{t}}{\mathrm{d}s}+\frac{\boldsymbol{n}}{r}\frac{\mathrm{d}z}{\mathrm{d}s}\right]-p_a\boldsymbol{n}+St\,z\,\boldsymbol{n}\quad\text{on } S_f,\tag{2.3}$$

where $Ca\equiv\mu U/\gamma$ is the capillary number, the local unit normal vector $\boldsymbol{n}$ at the free surface points from the liquid into gas, the local unit tangent vector $\boldsymbol{t}$ points in the direction of increasing s (from the bubble nose) along the free surface and relates to $\boldsymbol{n}$ in such a way that $\boldsymbol{n}\times\boldsymbol{t}=\boldsymbol{e}_\theta$ (with the right-handed coordinate system (z, r, θ) used in the present work). The constant excess pressure inside the bubble p_a is solved as an unknown to satisfy an overall constraint that the volume enclosed by the free surface S_f does not vary

$$\int_{S_f} r^2\frac{\mathrm{d}z}{\mathrm{d}s}\,\mathrm{d}s=\frac{4}{3}R_b^3,\tag{2.4}$$

where R_b denotes the volume-equivalent radius of the bubble. The Stokes number $St\equiv\rho\,g\,R^2/(\mu U)$ represents the buoyancy force and is also solved as an unknown to satisfy another overall constraint that the 'centre of mass' of the bubble remains at

† Here, the signs in front of p_a and St are different from those in the corresponding equation presented by Feng (2007), so that both p_a and St consistently take positive values.

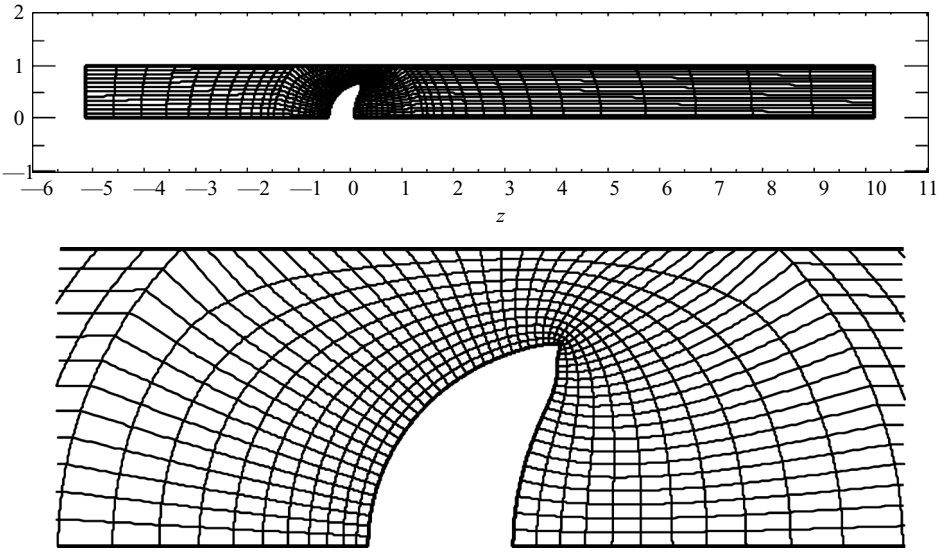

FIGURE 1. Finite-element mesh of the problem domain for $R_b = 0.5$ (shown for the case of $Re = 200$ and $We = 100$).

the coordinate origin

$$\int_{S_f} z\, r^2 \frac{\mathrm{d}z}{\mathrm{d}s}\, \mathrm{d}s = 0. \tag{2.5}$$

The gravitational (body) force term does not explicitly appear in (2.1) because the hydrostatic pressure in the bulk liquid has been lumped in the generalized pressure p (also called piezometric pressure). Hence, the hydrostatic pressure effect due to buoyancy force only appears in the boundary condition (2.3) through St.

Moreover, the flow velocity field must satisfy

$$\boldsymbol{n} \cdot \boldsymbol{v} = 0 \quad \text{on } S_f \text{ and } r = 0, \tag{2.6}$$

at the free surface S_f, due to the kinematic condition, and at the axis of symmetry ($r = 0$), as required by the symmetry condition. In addition, the stress-free symmetric condition at the axis of symmetry ($r = 0$) can be expressed as

$$\boldsymbol{e}_z \boldsymbol{e}_r : \boldsymbol{T} = 0 \quad \text{at} \quad r = 0, \tag{2.7}$$

where $\boldsymbol{e}_z$ and $\boldsymbol{e}_r$ denote the unit vectors in the z- and r-directions, respectively.

At the tube wall ($r = 1$) and the upstream (or 'inlet') boundary (e.g. located at $z = -5$ in figure 1), the Dirichlet type of condition for uniform flow velocity is imposed, i.e.

$$\boldsymbol{v} = \boldsymbol{e}_z \quad \text{on } r = 1 \text{ and } S_{inlet}. \tag{2.8}$$

At the downstream (or 'outflow') boundary (e.g. located at $z = 10$ in figure 1), the fully developed flow condition for hydrodynamic stresses is used, i.e.

$$\boldsymbol{e}_z \boldsymbol{e}_r : \boldsymbol{T} = \frac{\partial v_z}{\partial r} \text{ and } \boldsymbol{e}_z \boldsymbol{e}_z : \boldsymbol{T} = 0 \quad \text{on } S_{outlet}. \tag{2.9}$$

As described by Feng (2007), solutions of this problem can be computed by discretizing the partial differential equation system (2.1)–(2.9) with the Galerkin method of weighted residuals using finite-element basis functions (cf. Strang & Fix 1973; Kistler & Scriven 1984). The distribution of finite-element mesh points

around the deformable bubble surface is determined by a pair of elliptic partial differential equations that are also discretized by the Galerkin finite-element method (cf. Christodoulou & Scriven 1992; de Santos 1991). Then, the set of nonlinear algebraic equations of the Galerkin weighted residuals is simultaneously solved by Newton's method of iterations (Ortega & Rheinboldt 1970). At each Newton iteration, the Jacobian matrix of sensitivities of residuals to unknowns is evaluated with the values of unknowns determined in the previous iteration. The resulting linear algebra system is then solved by direct factorization of the Jacobian matrix with a modified version of Hood's frontal solver (Hood 1976). The iteration is continued until the L_2 norm of the residual vector becomes less than 10^{-8}.

With the present mathematical formulation, the Reynolds number Re and capillary number Ca are the two independent parameters that can be conveniently specified, with St determined as part of the solution. Once Re, Ca, and St are given, other relevant dimensionless parameters associated with a solution can all be calculated in terms of them. For example, the Weber number We, Eötvös number Eo, Froude number Fr, and buoyancy Reynolds number Re_G (which is also called dimensionless inverse viscosity by Fabre & Liné 1992) can be evaluated according to

$$\left.\begin{aligned} We &\equiv 2\rho U^2 R/\gamma = Re\, Ca, \\ Eo &\equiv 4\rho g R^2/\gamma = 4\, St\, Ca, \\ Fr &\equiv U/\sqrt{2gR} = (1/2)\sqrt{Re/St}, \\ Re_G &\equiv 2\sqrt{2g\rho^2 R^3}/\mu = 2\sqrt{Re}\, St. \end{aligned}\right\} \tag{2.10}$$

Because of the non-dimensional form of governing equations adopted in the present work, each solution corresponding to a set of specified Re and Ca can represent numerous seemingly different fluid systems and bubble sizes by virtue of dynamical similarity (as discussed by Batchelor 1967).

3. Bubbles rising in relatively large tubes ($R_b < 1$)

When the bubble radius is smaller than that of tube, the bubble behaviour strongly depends upon the bubble size as illustrated in a recent numerical study by Mukundakrishnan *et al.* (2007) using a front-tracking finite-difference method coupled with a level contour reconstruction of the front. Hence, cases are presented in this section according to the value of the bubble volume-equivalent radius R_b.

Shown in figure 1 is a quadrilateral finite-element mesh for a deformed bubble (of a spherical-cap shape) in a relatively large tube, namely $R_b = 0.5$ at $Re = 200$ and $We = 100$ (for $Ca = 0.5$). It contains 966 elements and 4047 nodes, with 109 nodes along the bubble surface.

For the case of relatively strong surface tension, i.e. $Ca = 0.01$, at $Re = 0$, the bubble shape is almost spherical. The computed value of St for $R_b = 0.5$ is 38.665, very close to 38.527 predicted by Haberman & Sayre (1958) for a spherical bubble moving in a cylindrical tube of radius 2 times of the bubble radius. Thus, the upstream and downstream boundaries in the present problem domain are shown to be far enough even at the limit of Stokes flow.

At $Re = 100$ and $Ca = 0.1$, figure 2 shows the changes in flow structure and bubble shape as bubble radius R_b increases from 0.25 to 0.50, 0.75, and 0.90. For convenience of comparison and future reference, the contour values for streamfunctions shown in figures of the present work are typically 0, ± 0.001, ± 0.002, ± 0.005, ± 0.01, ± 0.02, ± 0.05, ± 0.1, etc. like those in Ryskin & Leal (1984). When the tube is much

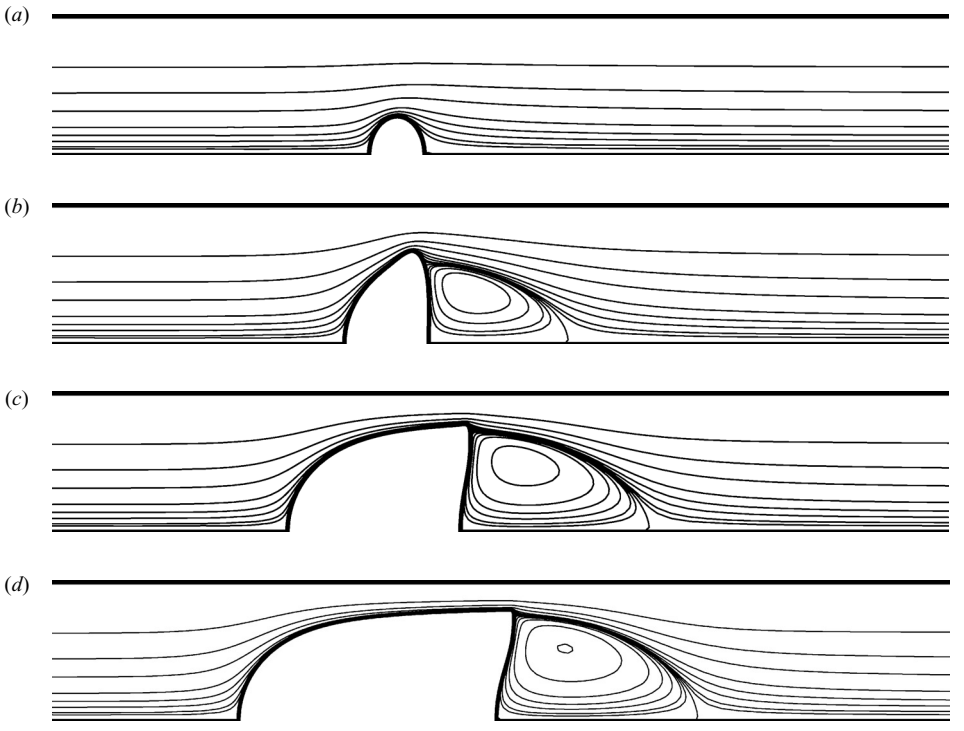

FIGURE 2. Streamlines and bubble shapes for (*a*) $R_b = 0.25$, (*b*) 0.50, (*c*) 0.75, and (*d*) 0.90 at $Re = 100$ and $Ca = 0.1$.

larger than the bubble (as in the case of $R_b = 0.25$), the bubble-size-based Reynolds number $Re_b \equiv R_b Re$ equals 25 for $Re = 100$ and the bubble-size-based Weber number $We_b \equiv Re_b\, Ca$ equals 2.5 for $Ca = 0.1$. The flow field around a slightly oblate bubble exhibits a similar structure to a case presented by Ryskin & Leal (1984) computed at Reynolds number 20 and Weber number 6 without flow separation.

As the bubble size is increased to $R_b = 0.5$, the values of Re_b and We_b become 50 and 5 (corresponding to $Re = 100$ and $Ca = 0.1$). The bubble develops a nearly spherical-cap shape. If a bubble is moving in an extended liquid, it is expected to take an oblate shape with a small toroidal vortex in the wake (cf. Ryskin & Leal 1984; Feng 2007). The nearly spherical-cap bubble shape formed at $Re_b = 50$ and $We_b = 5$ for $R_b = 0.5$ must be a consequence of the tube wall effect. Similar free-surface shapes were also observed for a drop of radius 0.5 and the same viscosity as that of the suspending liquid moving in a tube driven by a buoyancy force at about the same Reynolds number and capillary number (cf. Bozzi *et al.* 1997).

For bubbles with $R_b \geqslant 0.75$ (at $Re = 100$ and $Ca = 0.1$), the classical 'bullet' shape of long bubbles is clearly developed with almost invariant bubble nose shape and wake structure. The computed values of St for $R_b = 0.75$ and 0.90 are both 234.86 (corresponding to $Fr = 0.3263$), whereas St for $R_b = 0.25$ and 0.50 are 135.66 and 240.39 (corresponding to $Fr = 0.4293$ and 0.3225). It is interesting to note that even for a bubble of (volume-equivalent) radius half of the tube radius ($R_b = 0.5$) that is not shaped quite like a classical bullet as long bubbles, its buoyancy-driven terminal velocity can be virtually the same as those larger bubbles in the same tube (at $Re = 100$ and $Ca = 0.1$). Because the buoyancy Reynolds number Re_G for $R_b \geqslant 0.5$ is greater than 300, a value of $Fr = 0.3300$ (or 0.3393) is obtained from the universal

correlation formula of Viana *et al.* (2003) for long bubbles†

$$Fr = \begin{cases} \dfrac{0.009494\, Re_G^{1.026}}{(1+6197/Eo^{2.561})^{0.5793}}, & Re_G < 10, \\ \dfrac{0.34/(1+3805/Eo^{3.06})^{0.58}}{\left\{1+\left[\dfrac{31.08}{Re_G}\left(1+\dfrac{778.76}{Eo^{1.96}}\right)^{0.49}\right]^{1.45\left(1+\frac{7.22\times10^{13}}{Eo^{9.93}}\right)^{0.094}}\right\}^{0.71\left(1+\frac{7.22\times10^{13}}{Eo^{9.93}}\right)^{-0.094}}}, & Re_G \geqslant 10, \\ \dfrac{0.34}{(1+3805/Eo^{3.06})^{0.58}}, & Re_G > 200 \text{ and } Eo \geqslant 5, \text{ or } Re_G > 300 \text{ and } Eo \geqslant 3.5 \end{cases} \tag{3.1}$$

when the one for $Re_G \geqslant 10$ (or the one for $Re_G > 200$ and $Eo > 5$) is used based on $Re_G = 300$ and $Eo = 94$. Thus, the correlation formula of Viana *et al.* (2003) appears to be applicable even for bubbles barely forming the bullet shape in a round tube.

3.1. *Bubbles of* $R_b = 0.25$

A bubble moving through a liquid in a relatively large tube is expected to behave similarly to those in an extended liquid, for which Feng (2007) computationally predicted obtaining spherical-cap bubbles as Re_b increases with Ca fixed at about unity. Figure 3 shows the streamlines and bubble shapes for $Re = 8$, 40, 160, and 400 (corresponding to $Re_b = 2$, 10, 40, and 100) at $Ca = 1$ for bubbles of $R_b = 0.25$.

Bubbles at relatively small Re exhibit little deformation with a flow field with few interesting features. Even at $Re = 40$ ($Re_b = 10$), the flow barely separates at the rear surface of the bubble with a nearly spherical-cap shape, very much like a case presented by Ryskin & Leal (1984) at $Re_b = We_b = 10$. The flow separation would disappear if the value of Ca were reduced to 0.5 (corresponding to $Eo = 272.49$). Futher reducing Ca to 0.33 at $Re_b = 10$ ($We_b = 3.3$) results in $Eo = 159.33$ and a bubble of oblate spheroid shape of aspect ratio 0.653, with a flow field similar to a corresponding case presented by Mukundakrishnan *et al.* (2007) for $Re_b = 9.8$ and $We_b = 3.0$ (at $Eo = 160$).

The typical spherical-cap shape with toroidal vortices in the laminar wakes is indeed formed for bubbles at $Re = 160$ and 400 (i.e. $Re_b = 40$ and 100), similar to the cases computed by Feng (2007) for bubbles moving in extended liquids for Reynolds number $Re_b > 10$ at $Ca \sim 1$.

Table 1 shows a list of computed parameters at $Ca = 1$ for $R_b = 0.25$, suggesting that the spherical-cap bubble characteristics become almost invariant for $Re_b > 40$,

† Actually, Viana *et al.* (2003) presented the formula in (3.1) for $Re_G > 200$ and $Eo > 5$ as for $Re_G > 200$ (without specifying the range of Eo), and the formula in (3.1) for $Re_G \geqslant 10$ as for a transition region $10 < Re_G < 200$ (see also Funada *et al.* 2005). But the numerical values of Fr computed with the formulae for $Re_G > 200$ and for $10 < Re_G < 200$ show little difference (within 10%) for $Eo \geqslant 5$ and $Re_G > 200$, or $Eo \geqslant 3.5$ and $Re_G > 300$. (The majority of the experimental data used by Viana *et al.* (2003) were at $Eo \geqslant 6$, with comments for $Eo < 6$ like "too much scatter is present". Several authors (cf. Gibson 1913; Barr 1926; Bretherton 1961; White & Beardmore 1962) showed that long bubbles would not move at Eo less than $\sim$3.5.) Therefore, the applicable parameter ranges presented here (one for $Re_G < 10$ and one for $Re_G \geqslant 10$ and another of much simpler form for $Re_G > 200$ and $Eo \geqslant 5$ or $Re_G > 300$ and $Eo \geqslant 3.5$) for the universal correlation formula of Viana *et al.* (2003) seem to be reasonable.

Re	Re_G	Fr	Eo	r_{max}	z_{min}	z_{max}	z_{wake}
8	52.110	0.1535	339.43	0.262	−0.233	0.200	–
40	155.80	0.2567	606.81	0.311	−0.186	0.127	0.225
80	283.79	0.2819	1.007×10^3	0.351	−0.165	0.117	0.526
160	539.30	0.2967	1.818×10^3	0.390	−0.151	0.111	0.908
280	913.83	0.3064	2.982×10^3	0.412	−0.143	0.101	1.273
400	1283.4	0.3117	4.117×10^3	0.422	−0.139	0.0946	1.512
600	1894.9	0.3166	5.984×10^3	0.430	−0.136	0.0901	1.759

TABLE 1. Values of Re_G, Fr, Eo, r_{max}, z_{min}, z_{max}, and z_{wake} for $8 \leqslant Re \leqslant 600$ at $Ca = 1$ for bubbles of $R_b = 0.25$.

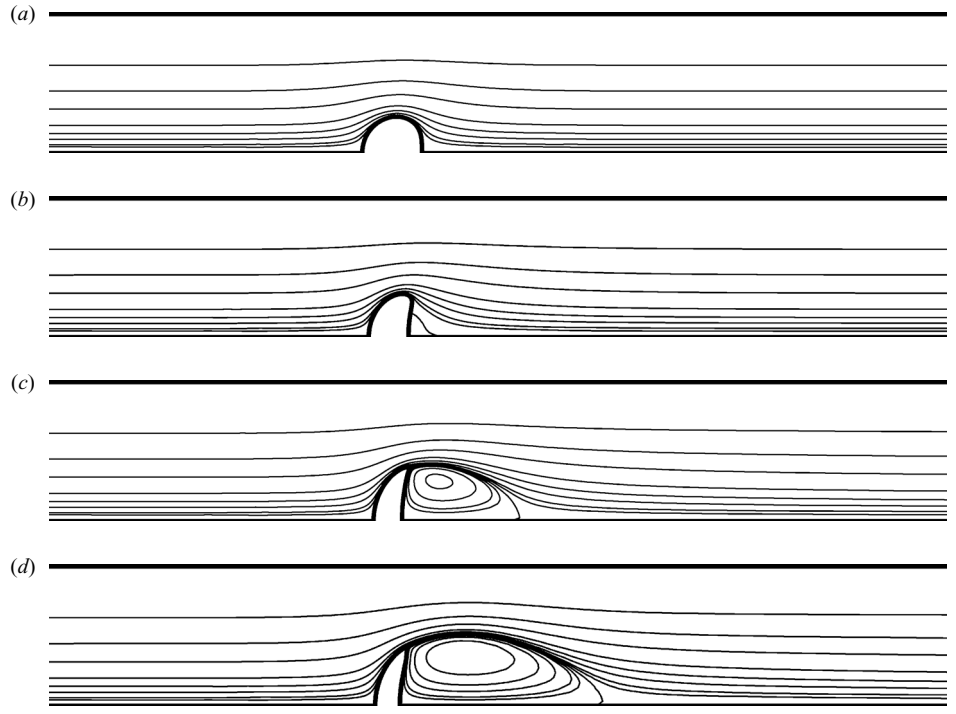

FIGURE 3. Streamlines and bubble shapes for (*a*) $Re = 8$, (*b*) 40, (*c*) 160, and (*d*) 400 at $Ca = 1$ and $R_b = 0.25$.

though the size of the toroidal vortex in the wake increases with Re_b, consistent with the findings of Feng (2007) for bubbles in extended liquids. As in Feng (2007), r_{max}, z_{min} and z_{max} denote the maximum r-coordinate, and minimum and maximum z-coordinate values of the deformable bubble surface, whereas z_{wake} is the z-value at the axis of symmetry where $v_z = 0$, indicating the end of the toroidal vortex in the wake.

Compared with the corresponding results of Feng (2007) for bubbles in extended liquids (at the same values of $Re_b = R_b\,Re$), the value of z_{wake}/R_b for bubbles of $R_b = 0.25$ is clearly smaller indicating shorter wake length due to the tube wall effect, a phenomenon also discussed by Mukundakrishnan *et al.* (2007) from a somewhat different perspective. For example, at $Ca = 1$ and $Re_b = 20$, 40, and 100 Feng (2007)

obtained $z_{wake}/R_b = 2.242$, 4.128, and 7.295, whereas the corresponding values from table 1 are $z_{wake}/R_b = 2.104$, 3.632, and 6.048. Noteworthy here is that the wake length reduction due to the tube wall effect becomes more significant (in percentage) as Re_b increases.

Many experiments have indicated that bubbles rising in an extended liquid with closed laminar toroidal wakes may only be observed for $Re_b < 200$ (Wegener & Parlange 1973; Hnat & Buckmaster 1976). For example, the results of Wegener & Parlange (1973) suggest that instability may set in when $Re_b > 180$, whereas Bhaga & Weber (1981) found the wake behind bubble becomes open and unsteady for $Re_b > 110$. Therefore, the cases with $Re > 600$ for $R_b = 0.25$ ($Re_b > 150$) may not be realizable in experiments despite the fact that they can still be computed numerically.

3.2. *Bubbles of* $R_b = 0.5$

As indicated in figure 2, a bubble of $R_b = 0.5$ seems to be ready to develop the basic characteristic behavior of long bubbles. According to many previous authors, the Froude number Fr becomes almost independent of Re_G for long bubbles with $Re_G > 200$ (cf. Viana *et al.* 2003). Thus, the terminal velocity of a long bubble in a tube of a given size is not expected to vary much, especially when Re_G is not small. For most liquids, the values of density ρ and surface tension γ do not vary more than a factor of 5, whereas viscosity μ can change by orders of magnitude. Hence, the value of We for long bubbles is primarily determined by the size of tube, whereas the value of Re (which is typically between $\sim 1/4$ and $1/3$ of the value of Re_G when the surface tension effect is relatively weak) for a given tube size reflects mostly the liquid viscosity effect. Evaluating the long-bubble behavior at a fixed value of We becomes almost equivalent to carrying out experiments with tubes of the same size.

Figure 4 shows the streamlines and bubble shapes for $Re = 20$, 100, 200, and 600 at $We = 50$ for bubbles of $R_b = 0.5$. Because the value of We is quite large, a sharply curved (almost cusp) surface develops at the bubble rim similar to those in spherical-cap bubbles computed by Feng (2007). Interestingly at $Re = 600$ (and $We = 50$), the bubble rim forms two sharply curved corners.

As in table 1, table 2 shows a list of computed parameters but for $We = 50$ for $R_b = 0.5$. Here the values of z_{wake}/R_b from table 2 (for $R_b = 0.5$) are further reduced from the corresponding values in table 1 (for $R_b = 0.25$) at the same Re_b. For example, at $Re_b = 100$ we have $z_{wake}/R_b = 4.040$ for $R_b = 0.5$ whereas 6.048 for $R_b = 0.25$. The value of Fr seems to become almost constant for $Re \geqslant 100$, corresponding to $Re_G > 300$ and $Eo > 400$, consistent with 0.34 computed with (3.1).

3.3. *Bubbles of* $R_b = 0.75$

Figure 5 shows the streamlines and bubble shapes for $Re = 20$, 100, 200, and 600 at $We = 20$ for bubbles of $R_b = 0.75$. Unlike the bubbles in figure 4 for $R_b = 0.5$ that still exhibit large-tube (or relatively small-bubble) characteristics such as a spherical-cap shape at $Re \sim 100$, 200, those for $R_b = 0.75$ in figure 5 start to develop the basic characteristics of the bullet shape of long bubbles. However, the rim with double sharp corners at $Re = 600$ with a pronounced concave bubble tail in figure 5 looks quite similar to the corresponding one (at $Re = 600$) in figure 4.

For comparison with tables 1 and 2, table 3 provides a list of computed parameters at $We = 20$ for $R_b = 0.75$. For $Re > 60$ (corresponding to $Re_G > 185$) the terminal velocity of the bubble approaches a constant value (~ 0.34) just as the formula (3.1) indicated (provided that Eo is not less than 40). Thus, it is not surprising to note that the computed Froude number Fr is 0.3263 for cases of $Re = 100$ and $We = 10$ shown

Re	Re_G	Fr	Eo	r_{max}	z_{min}	z_{max}	z_{wake}
10	42.494	0.2353	902.86	0.515	−0.488	0.423	0.472
20	71.071	0.2814	631.39	0.554	−0.446	0.381	0.558
60	187.73	0.3196	489.48	0.631	−0.397	0.318	1.025
100	305.32	0.3275	466.11	0.657	−0.385	0.280	1.378
200	598.60	0.3341	447.91	0.680	−0.375	0.241	2.020
600	1767.0	0.3396	433.65	0.694	−0.368	0.267	3.443

TABLE 2. Values of Re_G, Fr, Eo, r_{max}, z_{min}, z_{max}, and z_{wake} for $10 \leqslant Re \leqslant 600$ at $We = 50$ for bubbles of $R_b = 0.5$.

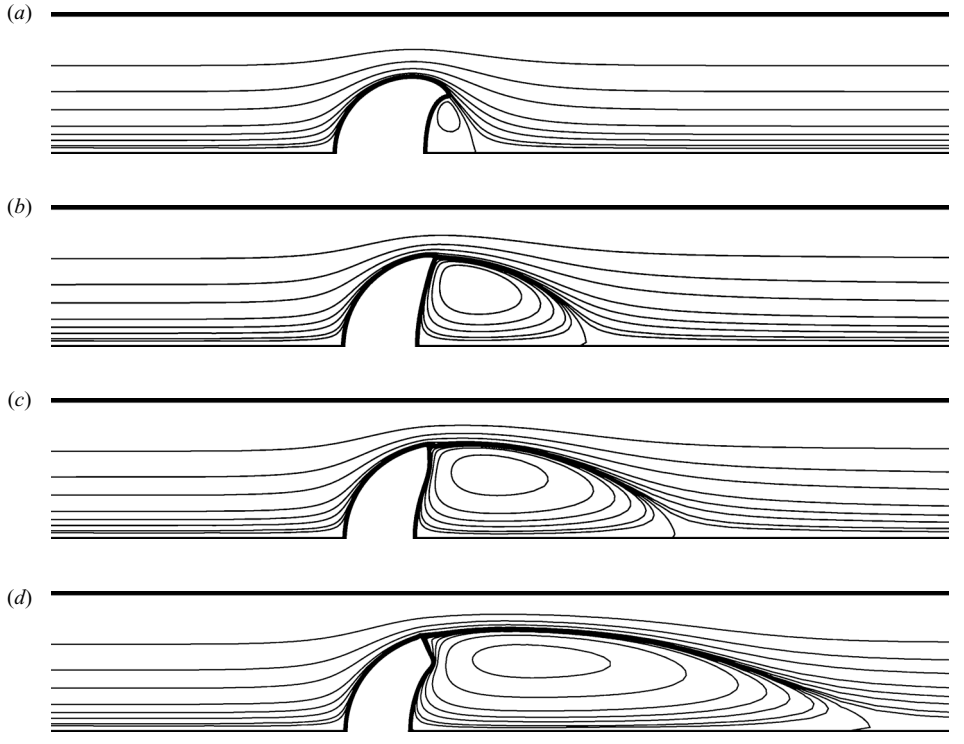

FIGURE 4. Streamlines and bubble shapes for (*a*) $Re = 20$, (*b*) 100, (*c*) 200, and (*d*) 600 at $We = 50$ and $R_b = 0.5$.

in figure 2 for $R_b \geqslant 0.75$, because the corresponding $Eo \sim 94 > 40$. Interestingly, the values of Froude number in table 3 are very close to the corresponding ones in table 2 despite the apparent difference in bubble shapes shown in figure 4 for $R_b = 0.5$ and figure 5 for $R_b = 0.75$.

4. Long bubbles rising in relatively small tubes ($R_b \geqslant 1$)

For long bubbles in relatively small tubes, it is more meaningful to discuss the bubble size in terms of bubble volume rather than of bubble radius R_b. A bubble of $R_b = 1$ has a volume of $4\pi/3$. Because the long-bubble behavior is expected to be somewhat independent of the bubble volume, cases are presented in this section at $We = 10$, 1.0, 0.1, etc. for different values of bubble volume $\geqslant 4\pi/3$.

Re	Re_G	Fr	Eo	r_{max}	z_{min}	z_{max}	z_{wake}
10	40.501	0.2469	328.07	0.661	−0.935	0.793	0.812
20	69.571	0.2875	242.01	0.695	−0.875	0.713	0.929
60	186.85	0.3211	193.97	0.750	−0.807	0.625	1.489
100	304.25	0.3287	185.14	0.770	−0.790	0.581	1.853
200	597.12	0.3349	178.27	0.794	−0.774	0.556	2.405
600	1764.5	0.3400	173.01	0.818	−0.765	0.607	3.063

TABLE 3. Values of Re_G, Fr, Eo, r_{max}, z_{min}, z_{max}, and z_{wake} for $10 \leqslant Re \leqslant 600$ at $We = 20$ for bubbles of $R_b = 0.75$.

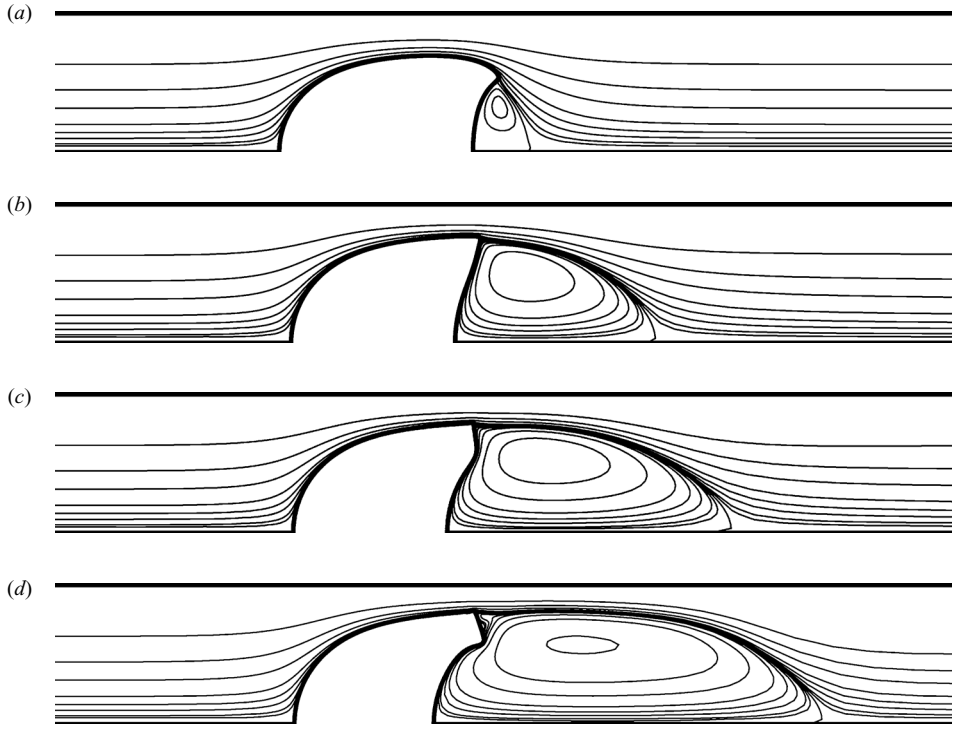

FIGURE 5. Streamlines and bubble shapes for (*a*) $Re = 20$, (*b*) 100, (*c*) 200, and (*d*) 600 at $We = 20$ and $R_b = 0.75$.

4.1. *Long bubbles at* $We = 10$

Figures 6, 7, and 8 show the streamlines and bubble shapes for volume $4\pi/3$, 2π, and 3π at $Re = 10$, 100, and 300, respectively. As many experiments have shown, bubbles of different volume (in the same liquid and tube) exhibit basically the same nose and tail profiles with similar wake structure; the only difference appears to be the length of the middle part consisting of a nearly uniform annular film attached to the tube wall. At a fixed value of Weber number $We = 10$, the bubble tail deformation becomes more pronounced with increasing Re whereas the bubble nose maintains almost the same round shape. A concave bubble tail deformation becomes obvious even at $Re = 10$, owing to the relatively weak surface tension effect at $We = 10$. Compared with the bubble in a larger tube (at a given value of Re), the tube wall effect tends to reduce the size of the toroidal vortex in the wake while

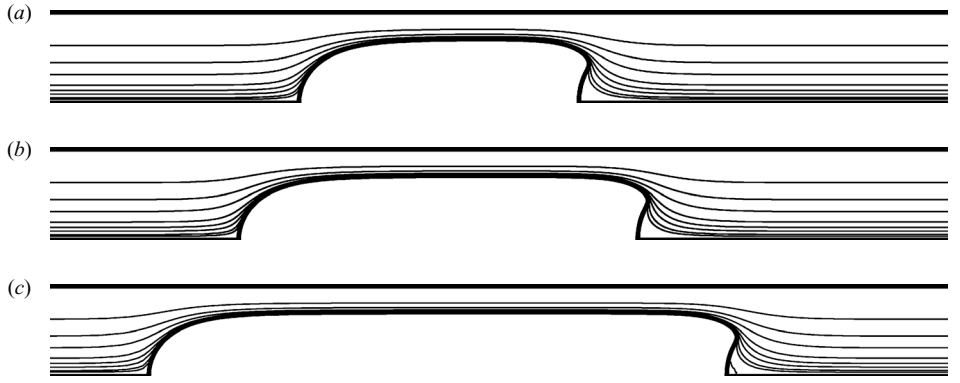

FIGURE 6. Streamlines and bubble shapes for bubble volume (*a*) $4\pi/3$, (*b*) 2π, and (*c*) 3π at $Re = 10$ and $We = 10$.

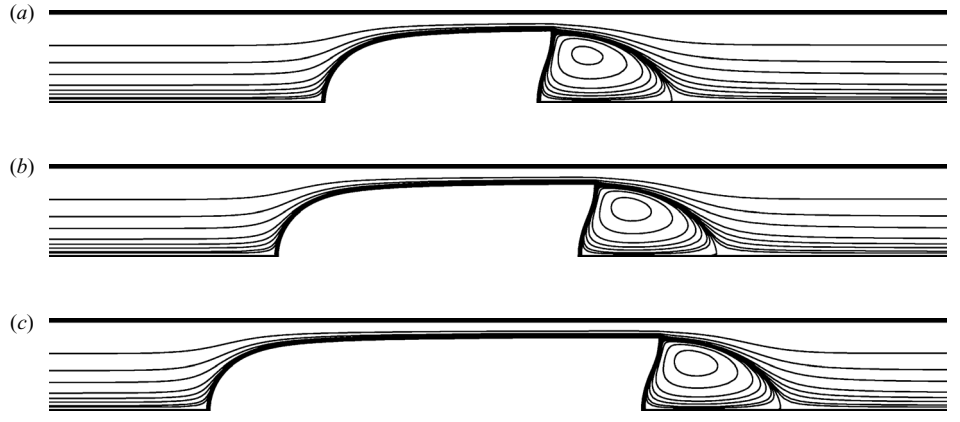

FIGURE 7. As figure 6 but at $Re = 100$.

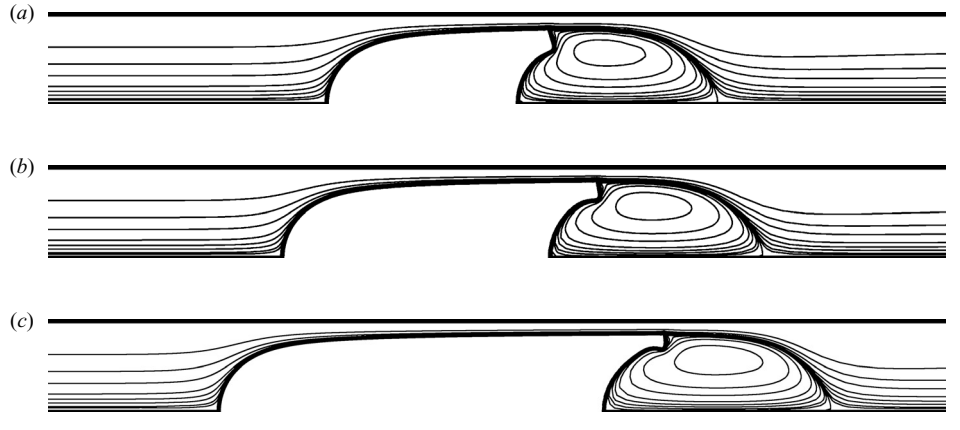

FIGURE 8. As figure 6 but at $Re = 300$.

enhancing the bubble tail deformation. At $Re = 300$, variations in bubble tail shape can be discerned for different bubble volumes (cf. figure 8), with more pronounced signature deformation for bubbles of larger volumes.

Volume	Re_G	Fr	Eo	$v_{z=0}$	$r_{z=0}$	v_{max}	r_{max}	z_{min}	z_{max}
$\frac{4}{3}\pi$	41.004	0.2439	168.13	2.538	0.7026	2.557	0.7045	−1.727	1.501
2π	41.019	0.2438	168.26	2.589	0.7074	2.595	0.7079	−2.399	2.157
3π	41.020	0.2438	168.27	2.599	0.7083	2.600	0.7084	−3.400	3.148

TABLE 4. Values of Re_G, Fr, Eo, $v_{z=0}$, $r_{z=0}$, v_{max}, r_{max}, z_{min}, and z_{max} for bubbles of volume $4\pi/3$, 2π, and 3π at $Re = 10$ and $We = 10$.

Volume	Re_G	Fr	Eo	$v_{z=0}$	$r_{z=0}$	v_{max}	r_{max}	z_{min}	z_{max}	z_{wake}
$\frac{4}{3}\pi$	306.49	0.3263	93.939	3.317	0.7865	4.087	0.8126	−1.445	1.111	2.439
2π	306.54	0.3262	93.964	3.732	0.8041	4.285	0.8203	−1.967	1.593	2.938
3π	306.53	0.3262	93.959	4.049	0.8163	4.289	0.8246	−2.726	2.312	3.652

TABLE 5. As table 4 but at $Re = 100$ with z wake added.

Volume	Re_G	Fr	Eo	$v_{z=0}$	$r_{z=0}$	v_{max}	r_{max}	z_{min}	z_{max}	z_{wake}
$\frac{4}{3}\pi$	893.27	0.3359	88.658	3.346	0.8063	5.701	0.8505	−1.397	1.137	2.961
2π	893.47	0.3358	88.698	3.927	0.8278	6.088	0.8632	−1.892	1.647	3.462
3π	893.48	0.3358	88.700	4.545	0.8449	6.512	0.8719	−2.599	2.378	4.223

TABLE 6. As table 5 but as $Re = 300$.

Although the computations of steady axisymmetric solutions can often be extended to $Re \geqslant 300$ with highly deformed bubble tails, some experiments indicated that axisymmetric bubbles in tubes with closed steady laminar toroidal wakes may only be observed for $Re < 200$ (cf. Campos & Guedes de Carvalho 1988), quite similar to the case of bubbles rising in an extended liquid (cf. Wegener & Parlange 1973; Bhaga & Weber 1981). For relatively short Taylor bubbles in tubes, capillary waves propagating from tail to nose were observed on the bubble surface (Nigmatulin & Bonetto 1997; Liberzon, Shemer & Barnea 2006). The analysis of Liberzon *et al.* (2006) supported the mechanism of pure capillary wave excitation from oscillatory open wakes in the unsteady bubble tail. Therefore, the computed steady axisymmetric solutions here for $Re > 200$ may not provide predictions of real observable phenomena, but rather satisfy theoretical curiosities.

Tables 4, 5, and 6 are lists of computed parameters for bubble volume $4\pi/3$, 2π, and 3π at $Re = 10$, 100, and 300, respectively. Although a bubble of volume $4\pi/3$ corresponds to $R_b = 1$, i.e. the volume-equivalent radius of the bubble is the same as the tube radius, it is ready to take a shape with nose and tail that is almost the same as those of larger bubbles of volume 2π and 3π. The values of Fr for $Re = 10$, 100, and 300 in tables 4, 5, and 6 agree well with the universal correlation formula of Viana *et al.* (2003) for $Re_G \geqslant 10$, which yields 0.235 (for $Re_G = 41$ and $Eo = 168$), 0.330 (for $Re_G = 306.5$ and $Eo = 94$), and 0.337 (for $Re_G = 893$ and $Eo = 88.7$). The flow structures around the bubble nose and bubble tail also appear to be invariant for $R_b \geqslant 1$. For example, the wake length $l \equiv z_{wake} - z_{max}$ for bubble volume $4\pi/3$, 2π, and 3π at $Re = 100$ is respectively 1.328, 1.345, and 1.340. At $Re = 300$, the wake length l becomes 1.824, 1.815, and 1.845 respectively for bubble volume $4\pi/3$, 2π, and 3π, with variations still rather insignificant despite the noticeable bubble tail shape differences.

If the annular liquid film has a constant thickness (as often assumed in theoretical treatments), the value of $r_{z=0}$ is expected to be the same as r_{max} and the film thickness

may be evaluated as $1 - r_{max}$. However, figures 6–8 indicate that the strictly uniform liquid film thickness may only be obtained at lower Re (i.e. $\leqslant 10$ for $We = 10$). Therefore, a comparison between $1 - r_{z=0}$ and $1 - r_{max}$ can be used to indicate the degree of general film uniformity, and as a basis for analysing local film flow. To faciliate further analysis, the tangential velocity of liquid flow along the free surface $v_{z=0}$ and v_{max} (usually located close to r_{max}) are also listed in tables 4–6. Apparently, the liquid film thickness as represented by either $1 - r_{max}$ or $1 - r_{z=0}$ decreases with increasing Re. The local tangential liquid flow velocity along the free surface v_{max} and $v_{z=0}$ increases with r_{max} and $r_{z=0}$ due to the conservation of mass.

Following the laminar film flow analysis of Brown (1965), by solving equation

$$\frac{1}{r}\frac{\partial}{\partial r}\left(r\frac{\partial u}{\partial r}\right) = \frac{\partial p}{\partial z} = -St, \tag{4.1}$$

where p denotes the piezometric pressure as in (2.1), with appropriated boundary conditions one could obtains

$$u = \frac{St}{2}\left(\frac{1 - r^2}{2} + \hat{r}^2 \ln r\right) + 1, \tag{4.2}$$

where $\hat{r} \leqslant r \leqslant 1$ with $\hat{r}$ denoting the radial coordinate of the local free surface of the uniform liquid film, as can be determined by considering conservation of mass

$$St\left[\tfrac{1}{4} - \hat{r}^2 + \hat{r}^4\left(\tfrac{3}{4} - \ln \hat{r}\right)\right] - 2\hat{r}^2 = 0. \tag{4.3}$$

For the case of $Re = We = 10$ where the annular draining film appears quite uniform, the computed values of St are basically identical, being equal to 42.03, 42.03, and 42.07, respectively for bubbles of volume $4\pi/3$, 2π, and 3π. (Consistent with (4.1) for a uniform annular draining film, the actual values of $\partial p/\partial z$ evaluated at $z = 0$ are -40.91, -41.84, and -42.06, within a few percent of the corresponding values of $-St$.). The values of $\hat{r}$ determined by (4.3) are 0.7083, 0.7084, and 0.7084, respectively. The corresponding values of $\hat{u}$ (calculated from (4.2) at $r = \hat{r}$) are 2.599, 2.600, and 2.600, respectively. Not surprisingly, the values of $r_{z=0}$ and $v_{z=0}$ as well as r_{max} and v_{max} in table 4 approach the theoretical values $\hat{r}$ and $\hat{u}$ for a perfectly uniform liquid film (determined from (4.2) and (4.3)) on increasing the long-bubble volume.

For the case of $Re = 100$ and $We = 10$, however, the bubble of volume 3π has the computed St value of 234.90 that leads to $\hat{r} = 0.8262$ and $\hat{u} = 4.331$, quite close to the values of r_{max} and v_{max} rather than $r_{z=0}$ and $v_{z=0}$ in table 5 because the liquid film thickness is not perfectly uniform. Further increasing Re to 300 (at $We = 10$) results in $St = 665.25$ for a bubble of volume 3π, which leads to $\hat{r} = 0.8747$ and $\hat{u} = 5.995$. Although the values of $\hat{r}$ and r_{max} are about the same, the value of $\hat{u}$ is about 10% less than v_{max} in table 6, suggesting slightly enhanced non-uniformity in the annular draining liquid film.

To understand the insensitivity of long-bubble terminal velocity to the bubble length (or bubble volume), it can be instructive to examine the z-component of traction, or z-traction, T_z on the bubble surface, where

$$T_z \equiv \boldsymbol{e}_z \cdot (-p_a \boldsymbol{n} - \boldsymbol{n} \cdot \boldsymbol{T}) = -n_z\left[-(p - p_a) + 2\frac{\partial v_z}{\partial z}\right] - n_r\left(\frac{\partial v_z}{\partial r} + \frac{\partial v_r}{\partial z}\right), \tag{4.4}$$

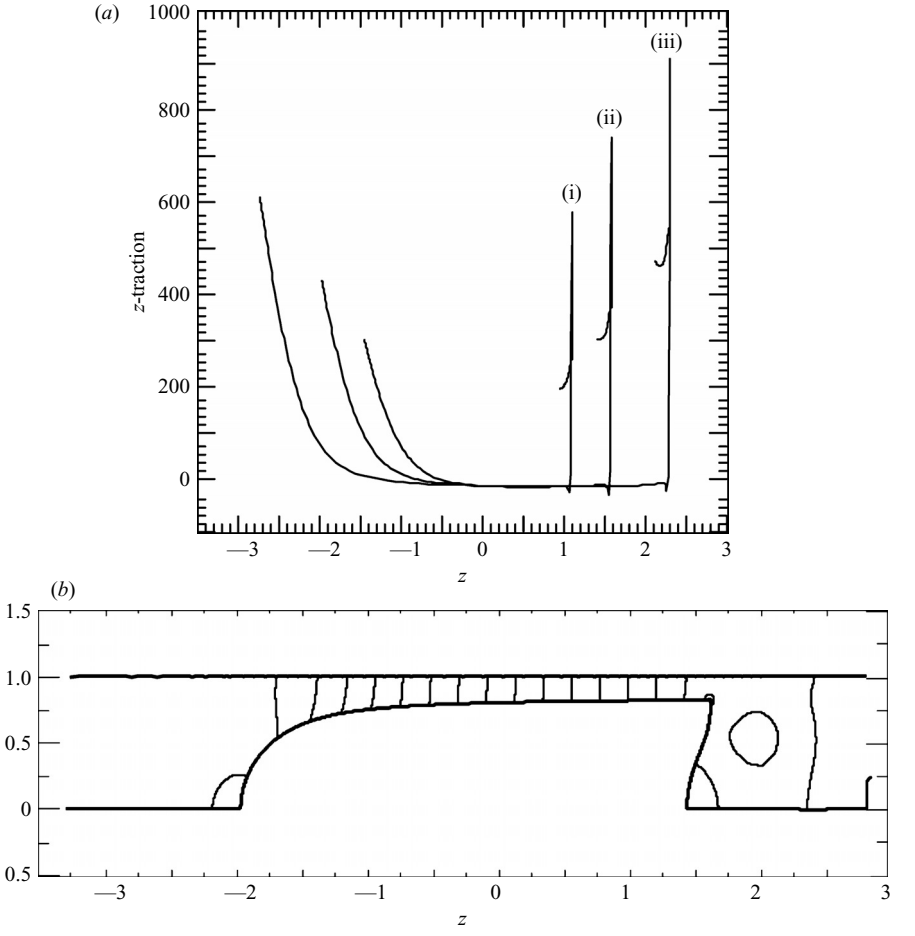

FIGURE 9. (*a*) The z-traction T_z along the bubble surface for bubbles of volume (i) $4\pi/3$, (ii) 2π, and (iii) 3π, and (*b*) pressure contours (from $p = -300$ to 700 in increments of 50) for a bubble of volume 2π at $Re = 100$ and $We = 10$.

with n_z, n_r denoting the z-, r-components of the local unit normal vector $\boldsymbol{n}$. Thus, the drag force can be computed by integrating T_z along the bubble surface as

$$2\pi \int_{S_f} T_z r \, \mathrm{d}s. \tag{4.5}$$

It should be noted that the constant excess pressure term p_a inside the bubble does not contribute to the integrated drag force; it only serves here as a common reference pressure for comparison purposes. The expression (4.4) makes it clear that in a uniform annular film where $n_z \sim 0$ and $n_r \sim 1$, the value of T_z must diminish because $\partial v_z/\partial r \sim 0$ due to the shear-free boundary condition and $v_r \sim 0$ due to (uniform) film flow (cf. Brown 1965). Thus, the drag force on the bubble mainly comes from the hydrodynamic stresses on the surface segments of the bubble nose and tail. This is shown in figure 9 with a plot of the z-traction T_z versus axial coordinate z along the bubble surface for volume $4\pi/3$, 2π, and 3π, and (piezometric) pressure contours around a bubble of volume 2π at $Re = 100$ and $We = 10$. As expected, T_z of significant magnitude can only be found on the bubble nose and tail. Moreover, the general

magnitude of T_z increases with the bubble volume, providing greater drag force to balance the buoyancy force for bubbles of greater volumes.

Because the flow velocity field $\boldsymbol{v}$ around the bubble nose and tail appears very similar for (long) bubbles of different volumes, the contribution of viscous stresses to the drag force must be independent of the bubble length. For the piezometric pressure field p, although a considerable gradient (with respect to z) appears along the draining liquid film, the local value of T_z remains almost negligible because of local $n_z \sim 0$ along a nearly uniform film. As indicated in (4.1), p is expected to decrease almost linearly with z along a draining liquid film, with a constant slope about $-St$ independent of bubble volume. Because the piezometric pressure p has the hydrostatic component subtracted out, its local gradient distribution around the bubble nose and tail, where the flow field and free surface shape are independent of bubble volume, are not expected to vary much for bubbles of different volumes. (The values of $p(z = z_{min}) - p(z = z_{min} + 1)$ around the bubble nose are 207, 210, and 211 respectively for bubble volume $4\pi/3$, 2π, and 3π, while those of $p(z = z_{max} - 1) - p(z = z_{max})$ are 158, 155, and 155.) Hence, it must be the gradient of p across the draining liquid film that is mainly responsible for adapting the local value of p (and thus the relative magnitude of T_z) around the bubble nose and tail, such that the integrated drag force is in the right proportion to the bubble volume to balance the buoyancy force. To illustrate this fact, values of $\Delta p/\Delta z$, where

$$\frac{\Delta p}{\Delta z} \equiv \frac{p(z = z_{max} - 1) - p(z = z_{min} + 1)}{z_{max} - z_{min} - 2} \tag{4.6}$$

is used here to measure the pressure gradient across the draining film length (for lack of a better definition), are evaluated as -228, -231, and -233 for bubble volume $4\pi/3$, 2π, and 3π, indicating a nearly constant pressure gradient. The slopes of p evaluated at $z = 0$ are -230.36, -232.90 and -234.09 for bubbles of volume $4\pi/3$, 2π, and 3π, still having a magnitude comparable to the corresponding values of $St = 234.85$, 234.91, and 234.90 despite the fact that the draining liquid film thickness is not perfectly uniform for $Re = 100$ and $We = 10$.

Therefore, an idealized long bubble may be considered as a circular cylinder of uniform cross-section connecting a nose and a tail. At a given set of Re and Ca, bubbles of different lengths differ only by the length of the cylinder but with identical nose and tail. The z-traction T_z is effectively zero on the free surface of a perfectly uniform cylinder, along which p decreases linearly in the flow direction with a slope of the same magnitude as St (i.e. the hydrostatic pressure gradient, as exemplified by a bubble of volume 3π at $Re = We = 10$ that has $\partial p/\partial z = -42.06$ at $z = 0$, $\Delta p/\Delta z = -42.06$, quite close to the computed $St = 42.07$). Hence, the difference in piezometric pressure across the length of the uniform cylinder exactly balances the cylinder portion of bubble volume contribution to the buoyancy force thereby the terminal velocity (i.e. the value of Fr) of a long bubble (with nearly uniform draining film) becomes independent of its length (or volume). When the draining liquid film is not substantially uniform (e.g. for cases of $Re \geqslant 100$ and $We = 10$), however, the value of $-\Delta p/\Delta z$ is reduced from that of St. In this case, the small contribution of T_z (because the conditions $n_z \sim 0$ and $n_r \sim 1$ may no longer be satisfied) along the surface of draining film to the drag force must compensate the reduced piezometric pressure difference across the draining film length to retain the bubble length independence of Fr. Thus, uniformity of the draining liquid film becomes an important indicator for determining whether a long bubble can be described well by the idealized long-bubble model.

On the surface of the annular draining liquid film where the curvature term $\boldsymbol{n}\cdot\mathrm{d}\boldsymbol{t}/\mathrm{d}s$ is expected to diminish and $\mathrm{d}z/\mathrm{d}s \sim 1$, (2.3) may be approximated by

$$r = \frac{1}{Ca\,[p_a - p - St\,z + 2\,\partial v_r/\partial r]}. \tag{4.7}$$

For flow in a perfectly uniform film, the value of $\partial v_r/\partial r$ should be zero. Thus, the relative magnitude of $\partial v_r/\partial r$ may also be a useful indicator of the draining film non-uniformity. For example, the computed values of $p_a - p(z=0)$ are 15.83, 14.13, and 13.03 respectively for bubbles of volume $4\pi/3$, 2π, and 3π (at $Re=100$ and $We=10$), whereas the corresponding local values of $\partial v_r/\partial r$ at $z=0$ are -1.225, -0.712, and -0.333, indicating the liquid film uniformity improves with increasing bubble volume. Substituting these values in (4.7) yields $r(z=0)=0.75$, 0.79, and 0.81, whereas the numerical solutions of $r(z=0)$ are actually 0.79, 0.80, and 0.82, respectively for bubbles of volume $4\pi/3$, 2π, and 3π, consistent with film uniformity improving with increasing bubble volume.

Of particular interest for theoretical analysis is the radius of mean curvature at the bubble nose (often called frontal radius), which can be determined by

$$R_{frontal} = \frac{2}{Ca\,[p_a - p - St\,z + 2\,\partial v_z/\partial z]} \quad \text{at } z = z_{min}. \tag{4.8}$$

For bubbles of volume $4\pi/3$, 2π, and 3π, the values of $R_{frontal}$ obtained according to (4.8) are 0.6499, 0.6504, and 0.6503, respectively (at $Re = 100$ and $We = 10$). The frontal radius appears to be significantly less than $r \sim 0.80$ at $z=0$, indicating a bubble nose of prolate-like rather than spherical shape as commented by Bugg *et al.* (1998) and also consistent with the findings of Funada *et al.* (2005) with the ovary ellipsoid approximation. At the centre of the bubble tail, the radius of local mean curvature can be calculated in a similar way as -0.9205, -0.8839, and -0.8542 for bubbles of volume $4\pi/3$, 2π, and 3π, respectively. This indicates that the bubble tail deformation is enhanced slightly as bubble volume increases, although the frontal radius of the bubble nose seems to be independent of bubble volume.

To successfully compute solutions for deformable long bubbles moving in round tubes, a suitable finite-element meshing scheme must be carefully set up. Figure 10 shows a few meshing examples (with 961 elements and 4053 nodes) for long bubbles of volume 3π at $Re=10$, 100, and 300. The mesh for a long bubble in figure 10 is constructed differently from that in figure 1 for bubbles in relatively large tube, to accommodate the long-bubble shape deformation. The present meshing scheme is shown to be capable of following various challenging free-surface deformations for a range of values of Re at $We=10$.

Although solutions for small Re (such as $Re=1$) can be computed at $We=10$, the local mesh distribution (without special adjustments) at the bubble tail may not be as desirable due to the highly localized concave deformation of the free surface. However, the computed values of Re_G, Fr, and Eo can be obtained respectively as 10.208, 0.0980, and 1041.9 for a bubble of volume 2π (at $Re=1$ and $We=10$), still in good agreement with the universal correlation formula given in (3.1) for $Re_G \geqslant 10$ that yields $Fr=0.0950$.

4.2. *Long bubbles (of volume 2π) at $We=1$*

Because the long-bubble behaviour in a tube does not seem to vary with the bubble volume (as shown in figures 6–8), cases with bubbles at a particular bubble volume 2π are expected to be reasonably representative. When the surface tension effect becomes

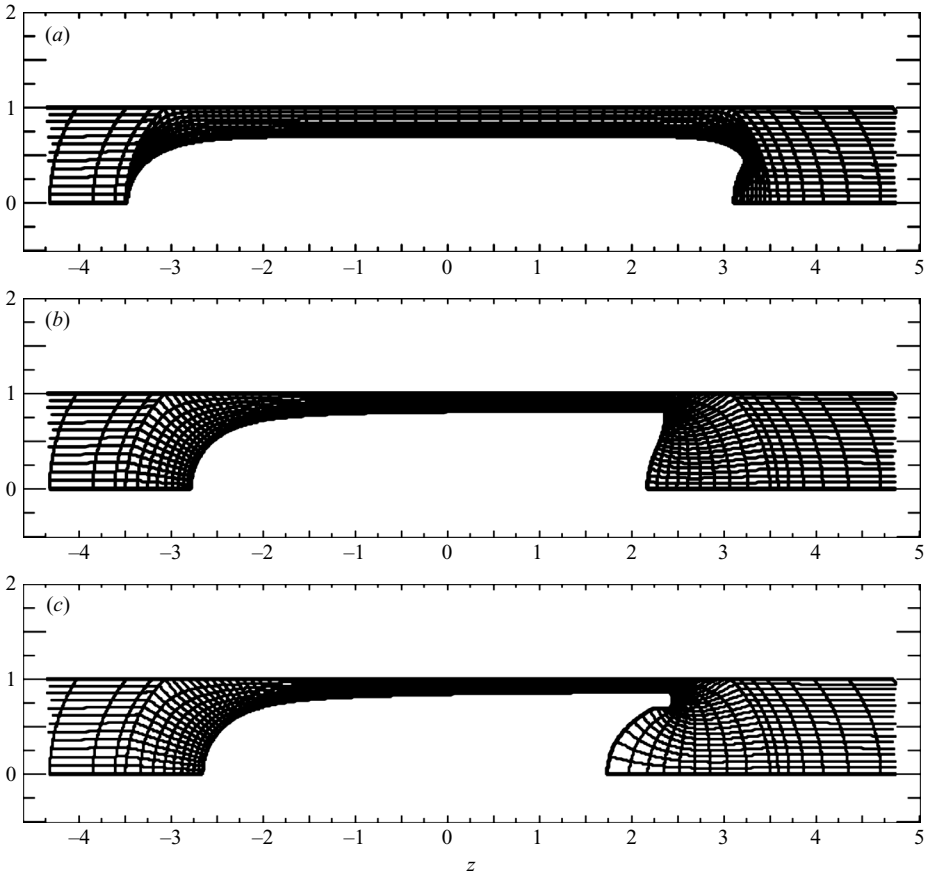

FIGURE 10. Mesh around a long bubble of volume 3π for (*a*) $Re = 10$, (*b*) 100, and (*c*) 300 at $We = 10$.

more important, the concave deformation at the bubble tail (commonly seen in cases at $We = 10$) disappears at $We = 1$ as shown in figure 11 for bubbles of volume 2π at various values of Re. Both the bubble nose and bubble tail take rather round (convex) shapes at $Re = 10$. But at $Re = 50$, a slightly bulging rim forms at the bubble tail. At $Re = 100$, the bulging rim becomes quite clear at the bubble tail where the free surface also shows a slight waviness along the drainage liquid film. The waviness of bubble tail deformation seen at $Re = 100$ becomes more pronounced at $Re = 300$. The significant surface tension effect resulting in non-uniformity (or unevenness) of the liquid film seems to be somewhat counter-intuitive; it indicates the complexity of nonlinear interaction between capillary surface curvature and inertial effect of drainage flow in the liquid film.

On the other hand, the stronger surface tension effect prevents high-curvature deformation at the bubble tail rim; consequently, flow separation does not occur until $Re > 75$ and the toroidal vortex in the bubble wake appears rather small for the case of $Re = 100$. Even at $Re = 300$, the toroidal vortex is still quite limited in size with streamlines concentrated toward the tube centreline, leaving an apparently stagnant annular region along the tube wall behind the bubble tail.

Table 7 shows the computed parameters for bubbles of volume 2π at various values of Re at $We = 1$. Compared with the case at $We = 10$, the value of Eo is considerably

Re	Re_G	Fr	Eo	$v_{z=0}$	$r_{z=0}$	v_{max}	r_{max}	z_{min}	z_{max}	z_{wake}
1	10.736	0.09314	115.27	2.336	0.6746	2.336	0.6746	−2.608	2.477	—
10	51.212	0.1953	26.227	2.928	0.7421	3.015	0.7523	−2.235	1.957	—
50	212.21	0.2356	18.014	3.944	0.8114	4.232	0.8238	−1.962	1.580	—
80	331.95	0.2410	17.217	4.275	0.8286	6.498	0.8893	−1.913	1.515	1.829
100	412.26	0.2426	16.996	4.443	0.8366	7.135	0.8994	−1.894	1.497	2.455
300	1209.3	0.2481	16.248	4.501	0.8516	9.765	0.9227	−1.851	1.466	2.868

TABLE 7. Values of Re_G, Fr, Eo, $v_{z=0}$, $r_{z=0}$, v_{max}, r_{max}, z_{min}, z_{max}, and z_{wake} for bubbles of volume 2π at $Re = 1$, 10, 50, 100, and 300 for $We = 1$.

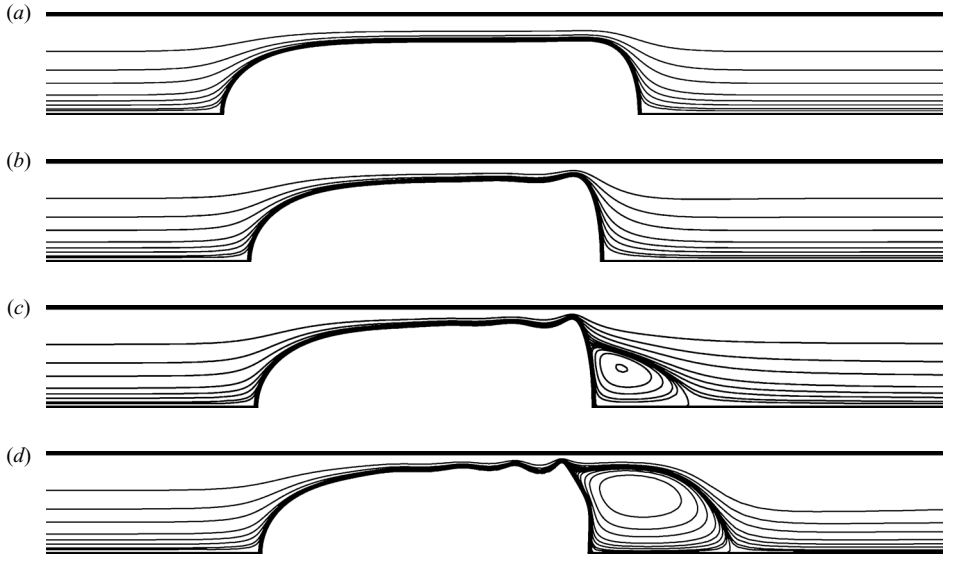

FIGURE 11. Streamlines and shapes of bubbles of volume 2π for (*a*) $Re = 10$, (*b*) 50, (*c*) 100, and (*d*) 300 at $We = 1$.

smaller at $We = 1$ and so is that of Fr as a consequence of stronger surface tension effect and thinner annular film for liquid drainage as indicated by greater r_{max} values in table 7. Owing to conservation of bubble volume, greater r_{max} also corresponds to a shorter bubble and higher tangential velocity v_{max}. The general agreement between the present computational results and (3.1) seems quite reasonable: substituting the values of Re_G and Eo into (3.1) for $Re_G \geqslant 10$ yields $Fr = 0.0963$, 0.203, 0.253, 0.252, 0.252, and 0.246 for $Re = 1$, 10, 50, 80, 100, and 300.

For the case of $Re = 1$ and $We = 1$, the values of r_{max} and v_{max} are basically the same as $r_{z=0}$ and $v_{z=0}$ in table 7, indicating the general uniformity of draining liquid film. Not surprisingly, (4.2) and (4.3) predict $\hat{r} = 0.6751$ and $\hat{u} = 2.341$ (based on the computed St of 28.817 for the bubble of volume 2π). The draining liquid film appears still quite uniform for the case of $Re = 10$ and $We = 1$ (cf. figure 11 and table 7). Therefore, the computed St of 65.657 leads to $\hat{r} = 0.7441$ and $\hat{u} = 2.954$, comparable to the values of r_{max} and v_{max} as well as $r_{z=0}$ and $v_{z=0}$ in table 7. For the case of $Re = 100$ and $We = 1$, however, the computed St is 424.89 that leads to $\hat{r} = 0.8556$ and $\hat{u} = 5.207$, taking values between r_{max}, v_{max} and $r_{z=0}$, $v_{z=0}$ (cf. table 7) due to the free surface waviness.

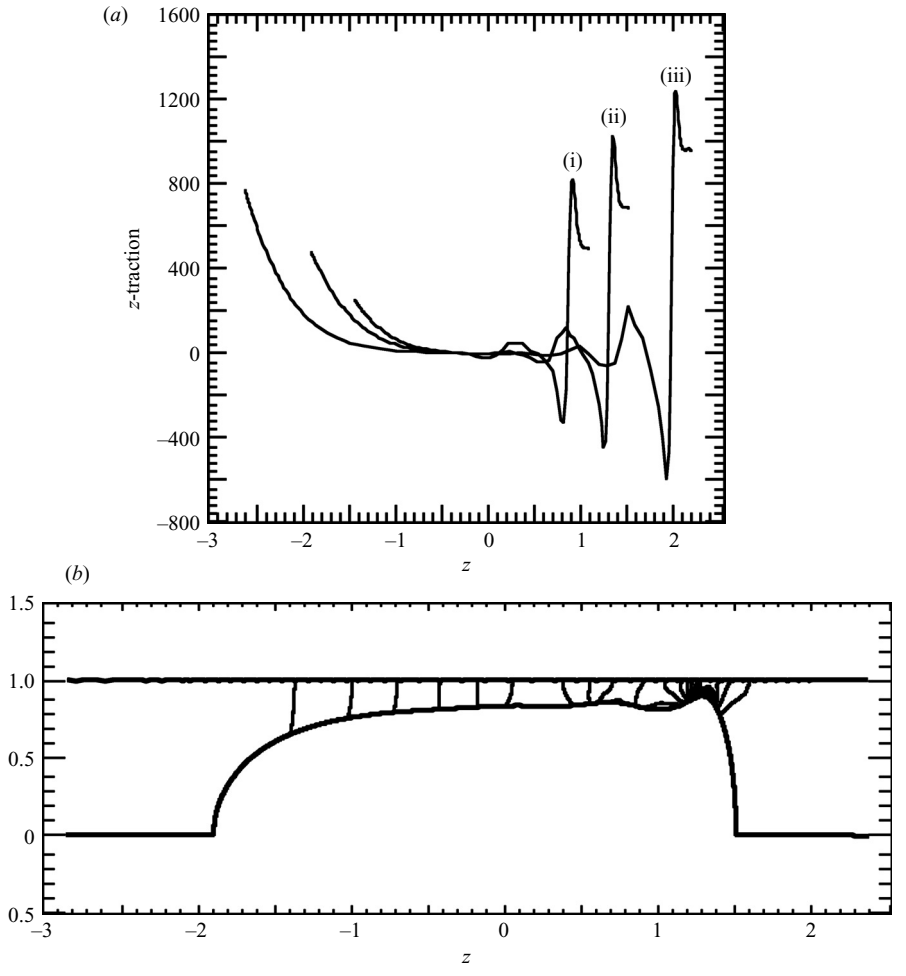

FIGURE 12. (*a*) The z-traction T_z along the bubble surface for bubbles of volume (i) $4\pi/3$, (ii) 2π, and (iii) 3π, and (*b*) pressure contours (from $p=-1300$ to 1100 in increments of 100) for a bubble of volume 2π at $Re=100$ and $We=1$.

As a comparison, the computed values of Fr for bubbles of volume $4\pi/3$ and 3π at $Re=100$ and $We=1$ are respectively 0.2474 and 0.2430, quite close to that for bubbles of volume 2π in table 7.

Similar to figure 9, figure 12 shows a plot of T_z versus z along bubble surfaces for volume $4\pi/3$, 2π, and 3π, and contours of p around a bubble of volume 2π at $Re=100$ and $We=1$. Despite some 'bumps' in the T_z profile toward the bubble tail as a consequence of the local waviness in the draining liquid film, values of T_z are still significant around the bubble nose and tail with greater amplitude of T_z for bubbles of larger volume. Thus, T_z over most of the draining liquid film region is expected to contribute little to the integrated drag force. Unlike figure 9 for $Re=100$ and $We=10$, the contours of p in figure 12 for $Re=100$ and $We=1$ appear somewhat uneven in the wavy liquid film, where the conditions $n_r\sim 1$ and $n_z\sim 0$ are not expected to be satisfied and T_z along the non-uniform liquid film is anticipated also to contribute to the integrated drag force. Not surprisingly, the values of $-\Delta p/\Delta z$ (cf. (4.6)) for bubbles of volume $4\pi/3$, 2π, and 3π, respectively equal 671, 389, and 385, whereas

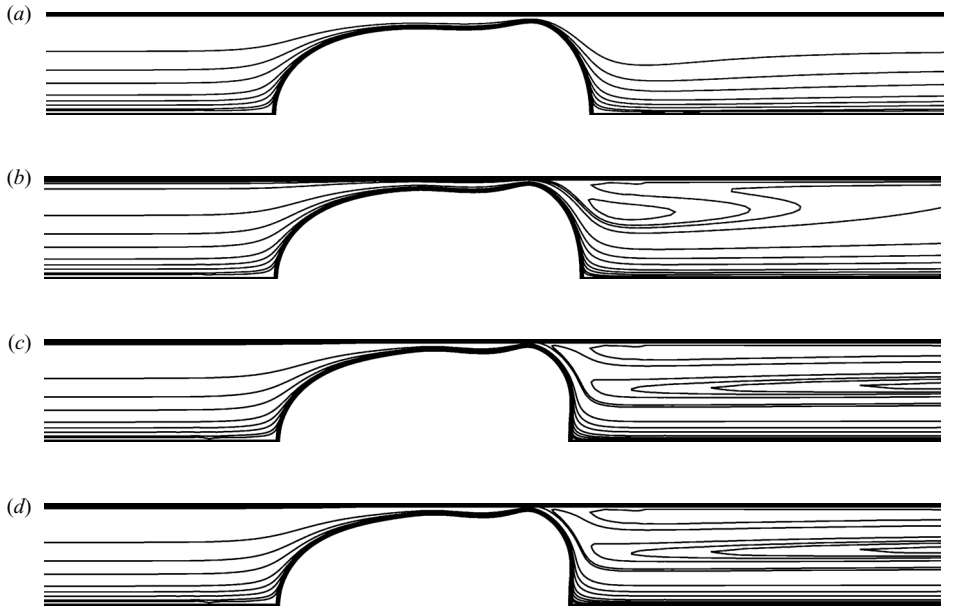

FIGURE 13. Streamlines and shapes of bubbles of volume 2π for (*a*) $Re = 50$, (*b*) 100, (*c*) 300, and (*d*) 500 at $We = 0.1$. A few contours of streamfunction are added for 0.4, 0.45, 0.47 in (*b*) and for 0.47, 0.57, 0.59, 0.60, 0.61, 0.62, and 0.63 in (*c*) and (*d*) to improve the visualization of the recirculation flow in the wake.

$St = 409$, 425, and 423. As expected, the bubble of volume $4\pi/3$ does not have much of a liquid film that can be described by the idealized draining film theory. Even for bubbles of volume $\geqslant 2\pi$, the value of $-\Delta p/\Delta z$ is reduced from that of St by about 10%. Thus, the idealized long-bubble model based on uniform film may need to be modified for describing bubbles with noticeable film non-uniformities.

4.3. *Long bubbles (of volume 2π) at $We = 0.1$*

At $We = 0.1$, figure 13 shows that along the free surface flow does not separate at all even up to $Re = 500$. However, recirculating eddies can appear (for $Re \geqslant 100$) in the bubble wake, not exactly associated with flow separation at the free surface but rather due to the curved high-speed stream emitted from the bubble's bulging rim that constricts the draining liquid flow to a narrow annular film and then suddenly releases the high-speed flow into a large space behind the bubble tail. Up to two toroidal recirculating eddies may be identified: one seems to be rather weak adjacent to the tube wall but slightly away from the bubble tail (as more apparent for cases of $Re = 300$ and 500), and the other appears relatively intense inside the bulk fluid. These recirculating eddies typically extend very far downstream and do not have streamlines connecting to the tube centreline or any boundaries. Relatively smaller curvature at the bubble tail rim at smaller We is expected to prevent flow separation from the free surface (cf. Batchelor 1967; Ryskin & Leal 1984). But the inertial effect at large enough Re combined with the shear-free condition along free surface tends to lead the streamlines toward the tube centreline, resulting in a vacuum zone immediately after the bubble rim bulge at the nearby solid tube wall. This type of complicated recirculating eddy in the bubble wake can only be expected in the presence of a nearby solid wall (where the no-slip boundary condition is observed) from which the flow deviates away due to curved free surface.

Re	Re_G	Fr	Eo	$v_{z=0}$	$r_{z=0}$	v_{max}	r_{max}	z_{min}	z_{max}
1	14.589	0.06854	21.284	2.768	0.7267	2.822	0.7342	−2.307	2.002
10	98.645	0.1014	9.7308	4.110	0.8166	5.489	0.8668	−1.889	1.646
50	448.33	0.1115	8.0400	5.596	0.8649	10.543	0.9315	−1.716	1.466
100	900.25	0.1111	8.1046	6.839	0.8894	13.339	0.9469	−1.675	1.398
300	2703.8	0.1110	8.1236	8.560	0.9191	15.524	0.9575	−1.654	1.296
500	4488.2	0.1114	8.0577	8.870	0.9266	15.835	0.9598	−1.650	1.280

TABLE 8. Values of Re_G, Fr, Eo, $v_{z=0}$, $r_{z=0}$, v_{max}, r_{max}, z_{min}, and z_{max} for bubbles of volume 2π at $Re = 1$, 10, 50, 100, 300, and 500 for $We = 0.1$.

Compared with the case at $We = 10$, the free surface of the annular liquid film is not as smooth, indicating that the thickness of draining liquid film is rather non-uniform at $We = 0.1$. However, the short-wavelength free-surface unevenness as seen in the case of $We = 1$ for $Re \geqslant 100$ disappears at $We = 0.1$ even up to $Re = 500$. There is a pronounced bulge at the bubble trailing surface forming the narrowest flow passage in the annular liquid film. But before reaching the bubble tail bulge, the liquid film thickness seems to be reasonably smooth and uniform, especially for $Re \leqslant 50$. As for that shown in figure 11, increasing Re (i.e. the inertial effect) tends to induce unevenness in the draining liquid film especially when $We \leqslant 1$.

Table 8 shows the computed parameters for bubbles of volume 2π at various values of Re at $We = 0.1$. Again the agreement between the present computational results and that of universal correlation formula by Viana *et al.* (2003) is quite reasonable. (Substituting the corresponding values of Re_G and Eo in (3.1) for $Re_G \geqslant 10$ yields $Fr = 0.0721$, 0.116, 0.106, 0.107, 0.108, and 0.106 for $Re = 1$, 10, 50, 100, 300, and 500, respectively.)

For the case of $Re = 1$ and $We = 0.1$, the bubble of volume 2π has the computed St of 53.210 that leads to $\hat{r} = 0.7277$ and $\hat{u} = 2.780$ (obtained from (4.3) and (4.2)), close to the values of $r_{z=0}$ and $v_{z=0}$ in table 8 because the draining liquid film is still reasonably uniform (at small Re) except around the bubble tail bulge where r_{max} and v_{max} are located. For the case of $Re = 10$ and $We = 0.1$, the computed St is 243.27 and the corresponding $\hat{r}$ and $\hat{u}$ are respectively 0.8281 and 4.378, also comparable to the values of $r_{z=0}$ and $v_{z=0}$ in table 8, indicating the validity of the laminar film flow theory of Brown (1965) based on the assumption of uniform film thickness. For the case of $Re = 100$ and $We = 0.1$, however, laminar film flow theory yields $\hat{r} = 0.9123$ and $\hat{u} = 8.557$, corresponding to the computed St of 2026.15, taking values between r_{max}, v_{max} and $r_{z=0}$, $v_{z=0}$ in table 8 as expected when the liquid film becomes considerably non-uniform (see figure 13).

A comparison among the data in tables 5, 7, and 8 for $Re = 100$ at $We = 10$, 1, and 0.1 reveals a clear trend of decreasing bubble length $L \equiv z_{max} - z_{min}$ (i.e. 3.560, 3.391, and 3.073) and increasing r_{max} (i.e. 0.8203, 0.8994, and 0.9469 for bubbles of volume 2π). As a consequence of narrowing the annular flow film, the value of Fr also decreases whereas the value of v_{max} increases on reducing We and Eo due to the enhanced surface tension effect.

Figure 14 shows a plot of the z-traction T_z versus axial coordinate z along the bubble surface for bubbles of volume $4\pi/3$, 2π, and 3π, and contours of p around a bubble of volume 2π at $Re = 100$ and $We = 0.1$. Compared with those in figures 9 and 12, the T_z distributions in figure 14 for $Re = 100$ and $We = 0.1$ indicate that a bubble of volume $4\pi/3$ may not share many characteristics of typical long bubbles because

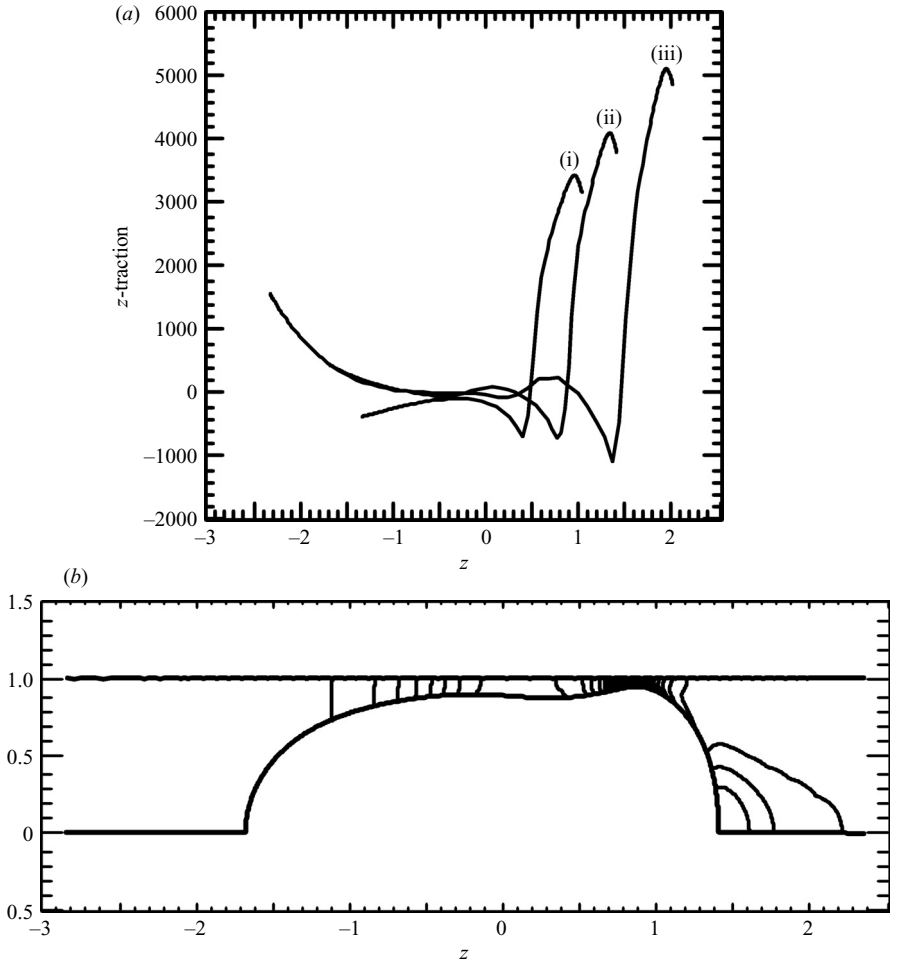

FIGURE 14. (*a*) The z-traction T_z along the bubble surface for bubbles of volume (i) $4\pi/3$, (ii) 2π, and (iii) 3π, and (*b*) pressure contours (from $p=-2000$ to 4400 in increments of 200) for a bubble of volume 2π at $Re=100$ and $We=0.1$.

T_z around its nose shows a dissimilar distribution from that for bubbles of larger volumes. Almost coincidentally T_z around the bubble nose for a bubble of volume 2π overlaps with that for a bubble of volume 3π. The non-uniformity of the annular draining liquid film is reflected by the fact that values of $-\Delta p/\Delta z=746$, 1074, and 1476, not even close to each other and differing significantly from the corresponding values of $St=2087$, 2026, and 1959 for bubbles of volume $4\pi/3$, 2π, and 3π. In this case, the uniform film flow theory (4.1) is no longer applicable. Thus, the analysis of flow in such a non-uniform draining liquid film and the mechanisms for bubbles of different volumes to rise at the same velocity is not expected to be as straightforward as that in § 4.1 for a relatively uniform film. Despite differences in detailed distribution profiles of T_z for bubbles at different values of We (for $Re=100$ as shown in figures 9, 12, and 14), it becomes quite clear that the value of T_z in (most of) the draining liquid film region is of insignificant magnitude (generally $<10\%$ if not negligibly small) compared with that around the bubble nose and tail. Even for bubbles with a quite non-uniform draining film along which T_z does not always vanish, the piezometric

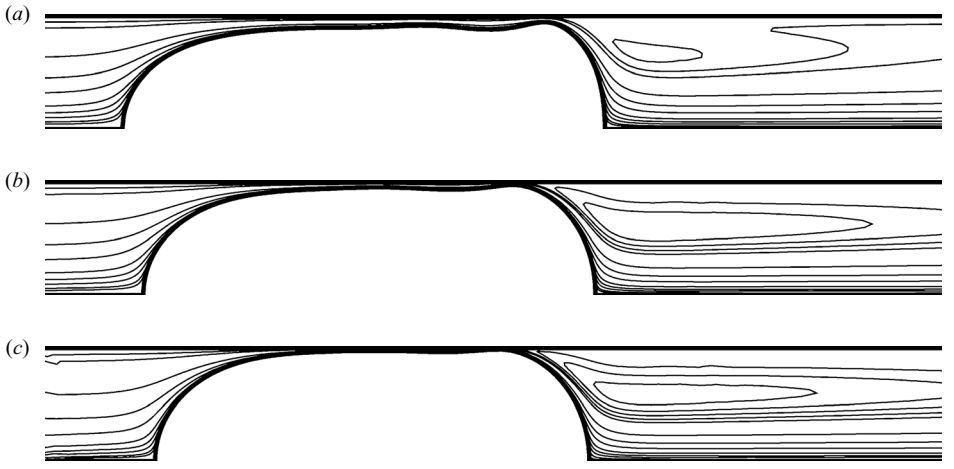

FIGURE 15. Streamlines and shapes of bubbles of volume 3π for $Re = 100$ at (*a*) $We = 0.1$, (*b*) 0.01 and (*c*) 0.001. A few contours of streamfunction are added at 0.4 and 0.45 in (*a*) at 0.4, 0.45, and 0.55 in (*b*), and at 0.4, 0.45, 0.55, and 0.6 in (*c*) to improve visualization of the recirculation flow in the wake.

pressure difference across the non-uniform film can still adapt the local magnitude of T_z around bubble nose and tail in the right proportion according to the bubble length, to ensure that the drag force balances the buoyant force on bubbles of different volumes with basically the same flow structure for a given set of Re and Ca.

With available solutions of p, St, p_a, and $2\partial v_z/\partial z$ respectively for bubble volume of $4\pi/3$, 2π, 3π at $Re = 100$ and $We = 0.1$, the corresponding $R_{frontal}$ according to (4.8) can be obtained as 0.6316, 0.6784, and 0.6765. At the centre of the bubble tail, the values for radius of local mean curvature are also calculated as 1.960, 2.104, and 2.084, respectively for bubble volume of $4\pi/3$, 2π, and 3π, suggesting that the bubble tail profile varies very little for bubbles of volume $\geqslant 2\pi$. According to (4.7), however, the radius of curvature at the annular film surface r at $z = 0$ would be 1.17, 0.80, and 0.99, whereas the numerical solutions of $r(z = 0) = 0.84$, 0.89, and 0.90, respectively for bubble volume of $4\pi/3$, 2π, and 3π. The physically unacceptable result of $r = 1.17 > 1$ for a bubble of volume $4\pi/3$ invalidates the assumptions behind (4.7) due to significant lack of film thickness uniformity.

Despite significant unevenness in the distribution of p along the bubble surface (see figure 14) due to relative strong surface tension influence, the computed values of Fr for bubbles of volume $4\pi/3$ and 3π at $Re = 100$ and $We = 0.1$ are respectively 0.1095 and 0.1130, surprisingly still quite insensitive to the bubble volume variation.

4.4. *Long bubbles (of volume 3π) at $We \leqslant 0.1$*

For cases of small Weber number with short bubble length, results for bubbles of volume 3π are illustrated here. Figure 15 shows streamlines around bubbles at $Re = 100$ for $We = 0.1$, 0.01, and 0.001. Not surprisingly, the streamline structure around a bubble of volume 3π at $We = 0.1$ is basically the same as that in figure 13 for a bubble of volume 2π at $Re = 100$ with a serpentine streamline in the wake. For $We = 0.01$ or smaller, the bubble shapes exhibit few free-surface features with nose and tail both round, except that the recirculating wake structure (seen in figure 13) is further enhanced with the thinning liquid film.

We	Re_G	Fr	Eo	$v_{z=0}$	$r_{z=0}$	v_{max}	r_{max}	z_{min}	z_{max}
0.1	885.19	0.1130	7.836	7.732	0.9047	13.332	0.9468	−2.308	1.994
0.05	1149.5	0.08699	6.607	9.869	0.9260	16.515	0.9583	−2.240	1.968
0.02	1682.9	0.05942	5.665	13.321	0.9445	24.720	0.9694	−2.170	1.934
0.01	2282.7	0.04381	5.211	16.312	0.9542	29.365	0.9764	−2.123	1.909
0.005	3114.7	0.03211	4.850	19.830	0.9624	38.204	0.9802	−2.084	1.890
0.002	4729.1	0.02115	4.473	26.028	0.9712	59.605	0.9870	−2.043	1.868
0.001	6520.9	0.01534	4.252	32.358	0.9767	73.365	0.9893	−2.018	1.854

TABLE 9. Values of Re_G, Fr, Eo, $v_{z=0}$, $r_{z=0}$, v_{max}, r_{max}, z_{min}, and z_{max} for bubbles of volume 3π at $Re = 100$ for $We = 0.1$, 0.05, 0.02, 0.01, 0.005, 0.002, and 0.001.

Table 9 shows the computed parameters for bubbles of volume 3π for various values of We at $Re = 100$. Substituting the values of Eo in (3.1) for $Re = 100$ yields $Fr = 0.102$, 0.0521, and 0.0367 for $We = 0.1$, 0.01, and 0.001. The agreement between the present computational values of Fr and those of the universal correlation formula (for $Re_G > 200$) by Viana *et al.* (2003) seems to deteriorate as $We < 0.02$ (and $Eo < 5.66$). This is not surprising because Viana *et al.* (2003) did not include the highly scattered data for $Eo < 6$ in their correlation construction. The values of v_{max} and r_{max} in table 9 for $We = 0.1$ are very much the same as those in table 8 for $Re = 100$, because the bubble tail bulge is expected to be independent of the bubble volume. However, the values of $v_{z=0}$ and $r_{z=0}$ (in table 9 for $We = 0.1$) differ noticeably from those in table 8 for $Re = 100$, indicating that the uniformity of the liquid film thickness can still be influenced by the bubble volume in the interval of 2π to 3π. Increasing the bubble volume tends to reduce the differences between $v_{z=0}$, $r_{z=0}$ and v_{max}, r_{max}.

The laminar film flow theory of Brown (1965) (i.e. (4.2) and (4.3)) predicts $\hat{r} = 0.9113$ and $\hat{u} = 8.466$ for computed $St = 1958.9$ for a bubble of volume 3π at $Re = 100$ and $We = 0.1$, improving the agreement with the corresponding values of $r_{z=0}$ and $v_{z=0}$ from those for a bubble of volume 2π (cf. table 8) because the liquid film thickness uniformity is expected to improve with longer bubbles. For a bubble of volume 3π at $Re = 100$ and $We = 0.01$, (4.2) and (4.3) yield $\hat{r} = 0.9521$ and $\hat{u} = 15.676$ for computed $St = 13026.8$, in reasonable agreement with the corresponding $r_{z=0}$ and $v_{z=0}$ in table 9. Even at $We = 0.001$ with computed $St = 106304$, the values of $\hat{r}$ and $\hat{u}$ calculated from the larminar film flow theory are respectively 0.9760 and 31.291, still comparing well with the corresponding $r_{z=0}$ and $v_{z=0}$ in table 9, indicating that the thickness of the annular liquid film must be reasonably uniform except around the free-surface bulge (characterized by r_{max} and v_{max}) toward the bubble tail when the surface tension effect becomes increasingly significant.

Although bubbles of smaller volumes do not share many of the characteristics (such as the value of frontal radius) of typical long bubbles, their rising velocity in the same tube and liquid seems to remain at about the same value as those bubbles of much larger volumes. As a check, the computed values of Fr for bubbles of volume $4\pi/3$ and 2π at $Re = 100$ and $We = 0.01$ are respectively 0.03931 and 0.04489, whereas at $We = 0.001$ they are 0.01533 and 0.01523, respectively.

4.5. *Comparison of long-bubble surface profiles with previous publications*

Despite the fact that long bubbles have been studied by numerous authors, well-documented images of complete bubble surface profiles with steady laminar flow can only be found in a few publications. For example, a couple of experimental bubble images are shown in Viana *et al.* (2003), with bubble surface profiles at relatively small

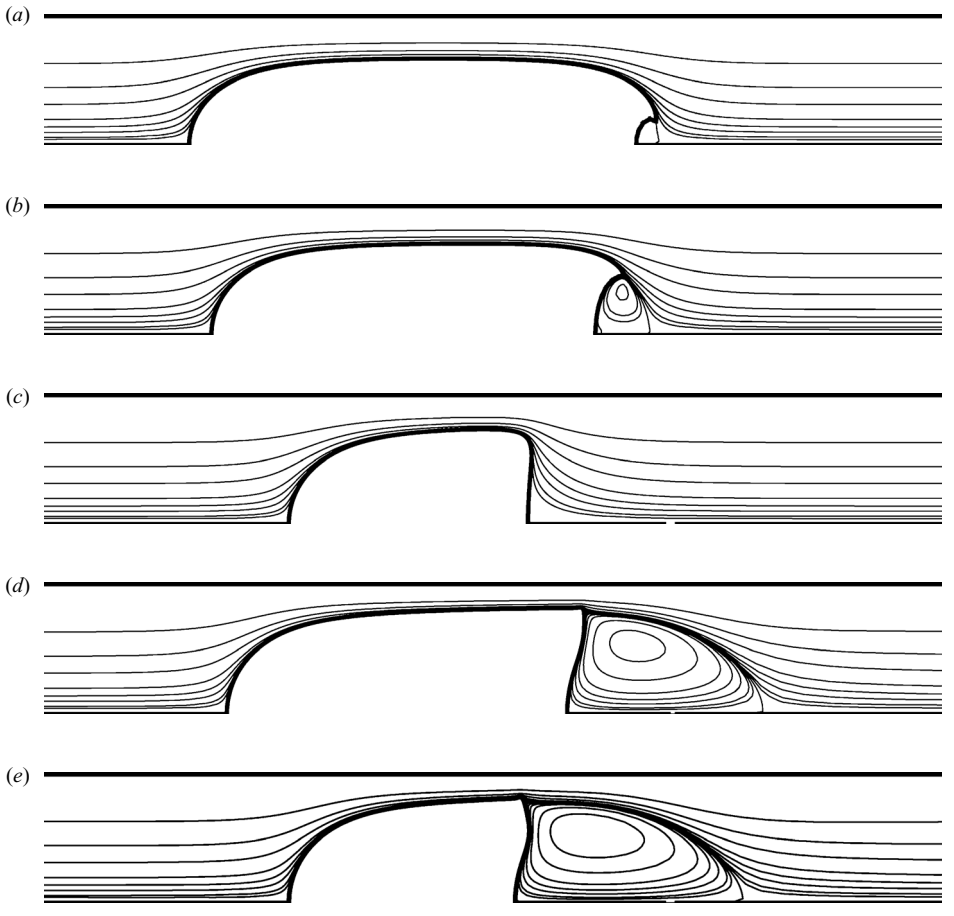

FIGURE 16. Streamlines and shapes of bubbles at (*a*) (*Re*, *Ca*) = (3, 10), (*b*) (13, 10), (*c*) (24, 0.2), (*d*) (106, 0.08), and (*e*) (160, 0.05), with corresponding volume $4\pi/3$, $4\pi/3$, $4\pi/5$, $3\pi/2$, and $46\pi/50$.

Re but large *Eo* having a tail that forms a gas 'cup' holding up a small mass of liquid. Campos & Guedes de Carvalho (1988) published a series of photographs visualizing flow in the steady laminar wake of long bubbles at $25 \leqslant Re \leqslant 180$ and $We > 5$; they found the wake becoming oscillatory for $Re > 180$ and turbulent at large values of *Re*. With a volume-of-fluid method, Tomiyama *et al.* (1996) computed twelve cases of long bubble shapes to compare with their own experiments for bubbles at relatively low *Re* (e.g. $\leqslant 90$) and *Eo* (e.g. <40). Bugg *et al.* (1998) presented computational bubble surface profiles in their figure 2 for the nine cases with tabulated parameter values.

Figure 16 shows a few bubble surface profiles with streamlines computed at $Re = 3$, 13, 24, 106, and 160 with $Ca = 10$, 10, 0.2, 0.08, and 0.05, respectively for bubbles of volume $4\pi/3$. $4\pi/3$, $4\pi/5$, $3\pi/2$, and $46\pi/50$. The results at $Re = 3$ and 13 for $Ca = 10$ (with $Re_G = 18.58$, $Eo = 1150.39$, $Fr = 0.1615$, and 48.60, 1817.14, 0.2675, respectively) are quite similar to the experimental cases at $Eo = 2600$ and $Re = 3$ and 13 (with corresponding $Fr = 0.1426$ and 0.2547) presented by Viana *et al.* (2003), where the bubble tails were found to form a gas 'cup' with liquid trapped therein. The computation becomes more difficult with increasing *Ca*; therefore no particular effort is made here to obtain solutions beyond $Ca = 10$. For the cases of (*Re*, *Ca*) = (24, 0.2),

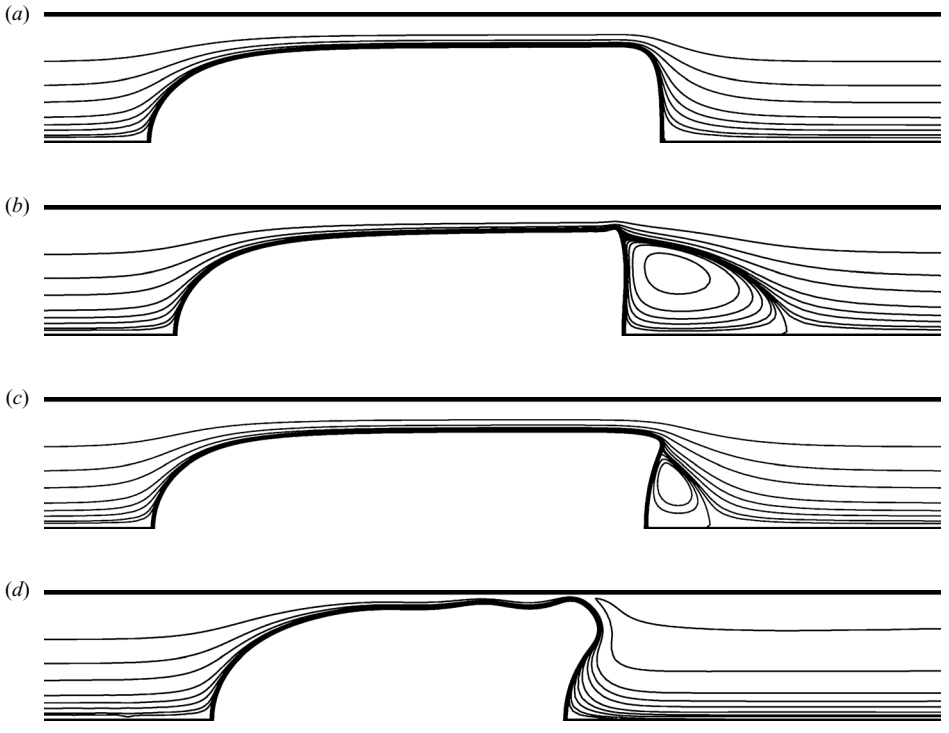

FIGURE 17. Streamlines and shapes of bubbles of volume 2π for (*a*) $Re = 21$ and $Ca = 0.12$, (*b*) $Re = 90$ and $Ca = 0.039$, (*c*) $Re = 30$ and $Ca = 0.3$, and (*d*) $Re = 850$ and $Ca = 1/2850$.

(106, 0.08), and (160, 0.05) with the values of bubble volume adjusted to produce bubble length $L = 1.892$, 2.787, and 1.874, the computed values of Re_G are respectively 85, 325, and 485 for comparison with the photographs of Campos & Guedes de Carvalho (1988) at $Re_G = 84$, 325, and 483 with corresponding bubble length $L = 1.895$, 2.737, and 1.895. The computed corresponding values of Fr are 0.2816, 0.3257, and 0.3298, which appears slightly smaller than those computed by Taha & Cui (2006) who reported $Fr = 0.30$ and 0.351 for $Re_G = 84$ and 325 but did not present results for $Re_G = 483$. For $(Re, Ca) = (106, 0.08)$ and (160, 0.05), the computed length of the toroidal vortex in the wake are $l = 1.390$ and 1.694, also comparable with those measured by Campos & Guedes de Carvalho (1988) of about 1.39 and 1.78.

Shown in figure 17 are surface profiles with streamlines for bubbles of volume 2π at $Re = 21$, 90, 30, and 850, with corresponding $Ca = 0.12$, 0.039, 0.3, and 1/2850, respectively. The cases at $(Re, Ca) = (21, 0.12)$ and (90, 0.039) with $(Re_G, Eo, Fr) = (81.1, 37.6, 0.259)$ and (294.8, 37.4, 0.306) have been computed for comparison with the corresponding computational cases of Tomiyama *et al.* (1996) at $Eo = 37.3$ for $Mo \equiv Eo^3/Re_G^4 = 1.26 \times 10^{-3}$ ($Re_G = 80.1$) and 6.92×10^{-6} ($Re_G = 294.3$), where the case of $Re_G = 80.1$ was shown to have no vortex in the wake whereas that of $Re_G = 294.3$ consisted of a small toroidal vortex of a length about 0.5. But the present computed result for the case at $Re_G = 294.8$ shows a wake with length $l = 1.24$. The case at $Re = 30$ and $Ca = 0.3$ with $(Re_G, Eo, Fr) = (100, 100, 0.2989)$ looks quite similar to the corresponding results computed by Bugg *et al.* (1998), which are also similar to the case of $Re = 27$ and $Eo = 100$ studied by Bugg & Saad (2002). However, the bubble surface profile computed with the Galerkin finite-element method here

at $Re = 850$ and $Ca = 1/2850$ with $(Re_G, Eo, Fr) = (5000, 10, 0.1700)$ does not have a convex oblate spheroidal tail like that obtained by Bugg *et al.* (1998) using the volume-of-fluid method for $Re_G = 5620$ and $Eo = 10$; it rather exhibits a similar profile to that in figure 13 for $Re = 500$ and $We = 0.1$ ($Ca = 1/5000$) with a concave tail. Some waviness along the liquid film appears adjacent to the tube wall, as expect when the value of Re is large while the surface tension effect is significant.

As a check, the values of Fr obtained from (3.1) are 0.299, and 0.146 for $(Re_G, Eo) = (100, 100)$ and $(5000, 10)$, respectively. A noticeable (>10%) discrepancy in Fr for the case of $Re_G = 5000$ and $Eo = 10$ occurs between the present computational result and (3.1). But $Fr = 0.179$ was reported by Bugg *et al.* (1998), computed at $Re_G = 5620$ and $Eo = 10$ to compare with 0.17 of White & Beardmore (1962), agreeing reasonably well with the present value of 0.170.

5. Summary and discussion

The solutions for buoyancy-driven steady axisymmetric motion of a gas bubble of various relative volumes through viscous liquid in a round tube are computed using a Galerkin finite-element method with a boundary-fitted mesh. Both the liquid flow field and free-surface profile can be determined with sufficient accuracy in great detail. Valuable information can then be revealed via systematically computed numerical solutions, as in the present work, for improving our understanding of the behaviour of bubbles, especially long (Taylor) bubbles, moving in a round tube.

When the bubble is relatively small compared with the tube size (e.g. $R_b \leqslant 0.25$), the bubble exhibits similar behaviour to that moving in an extended liquid, developing a spherical-cap shape with increasing Re for $Ca \sim O(1)$ (similar to that demonstrated by Feng 2007). The presence of the tube wall tends to reduce the size of the toroidal vortex in the wake. Although the shape of a bubble of $R_b = 0.5$ at various Re barely shows features of long bubbles (or Taylor bubbles), the values of (dimensionless) buoyancy-driven terminal velocity Fr are found to be much the same as those for larger bubbles (in the same tube and liquid). The basic long-bubble behaviour can often be readily seen in a bubble of $R_b = 0.75$ for most cases, especially when the surface tension effect is relatively weak. With the capability of the available computational code, only cases with significant bubble deformations at relatively large values of Eo and Re are presented in § 3 for $R_b < 1$. Cases of less deformed bubbles at relatively small Eo and Re can be found in recent front-tracking computations of Mukundakrishnan *et al.* (2007).

As the bubble volume-equivalent radius becoming comparable to the tube radius (e.g. $R_b = 1$ and therefore bubble volume equals $4\pi/3$), the bubble exhibits almost all the long-bubble characteristics, with nose and tail profiles as well as buoyancy-driven terminal velocity remaining (practically) similar to those for bubbles of greater volume. This finding is presented here by comparing the numerical results computed for bubbles of volumes $4\pi/3$, 2π, and 3π at various parameter settings.

If the surface tension effect is relatively weak (e.g. $We \geqslant 10$), long bubbles exhibit the typical bullet shape (as observed in many experiments) with an annular draining liquid film of smooth and nearly uniform thickness adjacent to the tube wall, especially at smaller Re (e.g. $\leqslant 100$) or for bubbles of considerably larger length (cf. figures 6 and 7). At $Re = 300$ (and $We = 10$), the bubble tail develops skirt-like shape (as in figure 8) with a profile varying slightly with the bubble length. The nearly uniform thickness of the liquid film adjacent to the tube wall is consistent with the analysis of laminar film flow by Brown (1965), who established the liquid film drainage theory to

explain many observed features of the long (Taylor) bubbles. The profiles of bubble nose and tail are found to be independent of bubble length when the bubble volume becomes $\geqslant 4\pi/3$ (for $We \geqslant 10$).

With a more significant surface tension effect (e.g. $We \leqslant 1$), however, the annular draining liquid film can become quite non-uniform especially at large Re (e.g. $\geqslant 50$ in figures 11 and 13); the draining liquid film, however, may appear to be uniform for $Re \leqslant 10$ at $We = 1$ (table 7), and for $Re \leqslant 1$ at $We = 0.1$ (table 8). The formation of a non-uniform liquid film is also reflected in the piezometric pressure distribution along the bubble surface (cf. figures 12 and 14 when compared with figure 9). The values of $r_{z=0}$ and r_{max} in table 9 show that even at very small We (e.g. $\leqslant 0.01$) with an extremely thin liquid film, the film thickness (i.e. $1 - r_{z=0}$ and $1 - r_{max}$) can vary by more than 50% due to the presence of a free-surface bulge toward the bubble tail. Yet, surprisingly, the computed values of Fr for bubbles of volume $4\pi/3$, 2π, and 3π still indicate that the bubble rising velocity remains (almost) independent of bubble length. In this case, the liquid film drainage theory of Brown (1965) based on the assumption of uniform film flow cannot be adequate for accurate analysis (especially for bubbles of volume $<2\pi$). The non-uniformity of the draining liquid film is found to have a noticeable influence on the local hydrodynamic traction distribution and its relative contribution to the integrated total drag force on a long bubble.

An examination of the detailed distributions of the z-component of traction (i.e. the z-traction) T_z on the bubble surface reveals that along most of the draining liquid film surface it provides a rather insignificant relative contribution to the integrated drag force on a long bubble. Only on the surface segments around the bubble nose and tail does T_z exhibit significant magnitudes. Therefore the drag force is mostly generated there. For bubbles of different lengths at the same Re and Ca, the profiles of T_z look similar due to virtually the same flow field around bubble nose and tail. However, the relative magnitude of the T_z profile differs for bubbles of different lengths, generally greater for a longer bubble. It is the piezometric pressure difference across the length of a (nearly uniform) draining liquid film that plays a major role in changing the magnitudes of the local value of p in T_z around the bubble nose and tail to the right proportion such that the drag force just balances the buoyancy force on a bubble of given length. An idealized long bubble may be considered as a circular cylinder of uniform cross-section connecting the nose and tail. Bubbles of different lengths differ only by the length of the cylinder while having identical nose and tail for a given set of Re and Ca. With the uniform draining liquid film described by (4.1) having a free surface with $n_z = 0$ and $n_r = 1$, the z-traction T_z is expected to vanish along the annular film surface where the piezometric pressure p decreases linearly with a slope equal to $-St$. Thus, the piezometric pressure difference across the length of the cylinder becomes exactly proportional to the cylinder length, generating a drag force according to the bubble length that just balances the buoyancy force. As a consequence, the rising velocity of long bubbles in the same liquid and same tube becomes independent of the bubble length. The uniformity of the draining film indicates how well the idealized long-bubble model can theoretically describe the independence of bubble rising velocity from bubble volume. Although the precise description of hydrodynamic mechanisms for a bubble with a non-uniform draining film may not be as clean and straightforward as that for an idealized long bubble (with a uniform film), similar analytical logic seems to be applicable.

Over a wide range of parameter values, the bubble nose exhibits a prolate-like shape, consistent with the finding of Funada *et al.* (2005) that an ovary ellipsoid (i.e. prolate spheroid) shape may be assumed for the bubble nose to derive a formula relating Fr

to Eo, Re_G, and ellipsoid aspect ratio. At $We = 10$ (when the surface tension effect is relatively weak), the frontal radius of about 0.65 for $Re = 100$ appears independent of bubble volume. But the computed bubble tail profile seems to vary as the bubble length changes (for bubbles of volume between $4\pi/3$ and 3π). Funada *et al.* (2005) demonstrated a very good fit to a set of normalized bubble nose profiles by Brown (1965) (from experiments at $We \geqslant 10$) with an ovary ellipsoid of aspect ratio 0.8 (minor vs. major axes, corresponding to a frontal radius $\sim$0.704).

The bubble nose profile data of Brown (1965) were obtained from experiments with bubbles in four different liquids: water, Varsol, Marcol, and Primol, corresponding to respective parameters (Re, We, Fr) $\sim$ (4500, 11, 0.346), (3500, 25, 0.342), (200, 20, 0.334), and (25, 15, 0.296). Among these experiments, the cases of Marcol and Primol are expected to have steady laminar flow without a turbulent wake, and are therefore computed here at (Re, We) (200, 20) and (25, 15) for a comparison. At $Re = 200$ and $We = 20$ (for bubble volume 3π), the computed Fr and the frontal radius $R_{frontal}$ are 0.335 and 0.685, whereas at $Re = 25$ and $We = 15$ they are 0.296 and 0.602. Brown (1965) also found that the free-surface profile in the bubble nose region is remarkably similar, even though elsewhere it can be significantly different depending on the fluid parameters; the frontal radius appears to be the same (about 0.75) for all liquids when normalized with the radius of the cylindrical part of the bubble (as given by $\hat{r}$ in (4.3) which has been shown to be very close to r_{max} for cases of $We \geqslant 10$). If the computed $r_{max} = 0.853$ and 0.750 are used as $\hat{r}$ at (Re, We) = (200, 20) and (25, 15), the corresponding values of $R_{frontal}/r_{max}$ for both cases are 0.803. For the case of $Re = 100$ and $We = 10$ analysed in § 4.1, the computed $R_{frontal} = 0.65$ and $r_{max} = 0.82$ lead to $R_{frontal}/r_{max} = 0.793$. For $Re = 10$, 50, and 300 at $We = 10$, we have $R_{frontal}/r_{max} = 0.768$, 0.797, and 0.774, respectively. Thus, the present computational results suggest that the normalized frontal radius $R_{frontal}/r_{max}$ is about 0.785 for $We \geqslant 10$ and $Re \geqslant 10$, slightly greater than the value of 0.75 suggested by Browm (1965) for the situation where both surface tension and viscous effects are relatively weak. This seems reasonable because in Brown's figure 3 – normalized bubble shape – most of the experimental data appear slightly above the arc of 0.75 radius.

When a sigificant surface tension effect is present, the difference in the value of frontal radius between bubbles of volume $4\pi/3$ and $\geqslant 2\pi$ may become more noticeable, even though the rising velocity is basically the same. For example, at $We = 0.1$ and $Re = 100$, the frontal radius is computed as $R_{frontal} = 0.6784$ and 0.6765 for bubbles of volume 2π and 3π, whereas $R_{frontal} = 0.6316$ is obtained for a bubble of volume $4\pi/3$. As shown by the computed results presented here for a given bubble volume, increasing We tends to increase the bubble length while increasing Re slightly reduces the bubble length. For the case of $Re = 100$ at $We = 0.1$, a bubble of volume $4\pi/3$ has a length $L = 2.361$ (<2.5) with a frontal radius ($R_{frontal} = 0.632$), noticeably different from that for bubbles of volumes $\geqslant 2\pi$ (0.677). In contrast, at $We = 1$ and $Re = 100$, the length of a bubble with volume $4\pi/3$ becomes 2.505 having a frontal radius $R_{frontal} = 0.604$, comparable to 0.610 for bubbles of volume $\geqslant 2\pi$. Another example is $We = 10$ and $Re = 300$, where the bubble with volume of $4\pi/3$ has a length 2.534 and a frontal radius $R_{frontal} = 0.673$, comparable to 0.674 for bubbles of volume $\geqslant 2\pi$. Thus, the minimum length for a bubble to retain the same value of frontal radius for long bubbles seems to be 2.5 as measured in units of the tube radius.

Although various steady axisymmetric solutions of deformable bubbles in round tubes are obtained at various values of Re and Ca, their stability cannot been easily examined within the present computational framework. Based on experimental

observations reported in the literature, bubbles in an extended liquid (or in large tubes) may become unstable with unsteady open wakes at $Re_b > 110$ (cf. Bhaga & Weber 1981) or $Re_b > 180$ (Wegener & Parlange 1973), whereas long bubbles in round tubes seem to develop oscillating wakes at $Re > 180$ (e.g. Campos & Guedes de Carvalho 1988) which may excite capillary waves propagating from tail to nose, especially on surfaces of relatively short Talyor bubbles (cf. Liberzon *et al.* 2006). Thus, the steady axisymmetric solutions at $Re_b > 200$ in § 3 and § 4, such as in figures 4 and 5 for $Re = 600$ and in figure 8 at $Re = 300$ with multiple sharp corners at the bubble rim, may not represent stable states observable in laboratory experiments. If not stable, these steady axisymmetric solutions cannot describe real observable phenomena; however, their existence may have some theoretical importance. Yet, interestingly, those solutions at large Re still predict values for bubble rising velocity in good agreement with the universal correlation formula of Viana *et al.* (2003), unstable though they might be. Owing to the nonlinear nature of the Navier–Stokes equation system, uniqueness of solutions is not guaranteed. It should not be surprising to find multiple steady axisymmetric solutions for deformable bubbles at a given set of Re and Ca, as demonstrated by Feng (2007). A thorough investigation of steady solutions in the parameter space with linear stability analysis can be a quite involved task, even though viable strategies have been illustrated (cf. Christodoulou 1989; Carvalho 1996). Therefore, investigation of the stability of computed steady axisymmetric solutions, especially for highly deformed bubbles at large Re, is left open for future research.

REFERENCES

Barr, G. 1926 The air bubble viscometer. *Phil. Mag.* (7), **1**, 395–405.

Batchelor, G. K. 1967 *An Introduction to Fluid Dynamics.* Cambridge University Press.

Bhaga, D. & Weber, M. E. 1981 Bubbles in viscous liquids: shapes, wakes and velocities. *J. Fluid Mech.* **105**, 61–85.

Bozzi, L. A., Feng, J. Q., Scott, T. C. & Pearlstein, A. J. 1997 Steady axisymmetric motion of deformable drops falling or rising through a homovisous fluid in a tube at intermediate Reynolds number. *J. Fluid Mech.* **336**, 1–32.

Brignell, A. S. 1973 The deformation of a liquid drop at small Reynolds number. *Q. J. Mech. Appl. Maths* **26**, 99–107.

Bretherton, F. P. 1961 The motion of long bubbles in tubes. *J. Fluid Mech.* **10**, 166–188.

Brown, R. A. S. 1965 The mechanics of large gas bubbles in tubes. *Can. J. Chem. Engng* **Q2**, 217–223.

Bugg, J. D., Mack, K. & Rezkallah, K. S. 1998 A numerical model of Taylor bubbles rising through stagnant liquids in vertical tubes. *Intl J. Multiphase Flow* **24**, 271–281.

Bugg, J. D. & Saad, G. A. 2002 The velocity field around a Taylor bubble rising in a stagnant viscous fluid: numerical and experimental results. *Intl J. Multiphase Flow* **28**, 791–803.

Campos, J. B. L. M. & Guedes de Carvalho, J. R. F. 1988 An experimental study of the wake of gas slugs rising in liquids. *J. Fluid Mech.* **196**, 27–37.

Carvalho, M. S. 1996 Roll coating flows in rigid and deformable gaps. PhD thesis, University of Minnesota.

Christodoulou, K. N. 1989 Computational physics of slide coating flow. PhD thesis, University of Minnesota.

Christodoulou, K. N. & Scriven, L. E. 1992 Discretization of free surface flows and other moving boundary problems. *J. Comput. Phys.* **99**, 39–55.

Clarke, A. & Issa, R. I. 1997 A numerical model of slug flow in vertical tubes. *Comput. Fluids* **26**, 395–415.

Clift, R. C., Grace, J. R. & Weber, M. E. 1978 *Bubbles, Drops and Particles.* Academic.

Collins, R. 1965 A simple model of the plane gas bubble in a finite liquid. *J. Fluid Mech.* **22**, 763–771.

Collins, R. 1966 A second approximation for velocity of a large gas bubble rising in an infinite liquid. *J. Fluid Mech.* **25**, 469–480.

Davies, R. M. & Taylor, G. I. 1950 The mechanics of large bubbles rising through extended liquids and through liquids in tubes. *Proc. R. Soc. Lond.* A **200**, 375–390.

Dumitrescue, D. T. 1943 Stromung nd einer luftbluse in senkrechten rohr. *Z. Angew. Math. Mech.* **23(3)**, 139–149.

Fabre, J. & Liné, A. 1992 Modelling of two-phase slug flow. *Annu. Rev. Fluid Mech.* **24**, 21–46.

Feng, J. Q. 2007 A spherical-cap bubble moving at terminal velocity in a viscous liquid. *J. Fluid Mech.* **579**, 347–371.

Funada, T., Joseph, D. D., Maehara, T. & Yamashita, S. 2005 Ellipsoidal model of the rise of a Taylor bubble in a round tube. *Intl J. Multiphase Flow* **31**, 473–491.

Gibson, A. H. 1913 Long air bubbles in a vertical tube. *Phil. Mag.* (6), **26**, 952–965.

Haberman, W. L. & Sayre, R. M. 1958 Motion of rigid and fluid spheres in Stationary and moving liquids inside cylindrical tubes. *David Taylor Model Basin Report* 1143.

Hnat, J. G. & Buckmaster, J. D. 1976 Spherical cap bubbles and skirt formation. *Phys. Fluids* **19**, 182–194.

Hood, P. 1976 Frontal solution program for unsymmetric matrices. *Intl J. Num. Meth. Engng* **10**, 379–399 (and corrigendum **11**, 1055 (1977)).

Joseph, D. D. 2003 Rise velocity of a spherical-cap bubble. *J. Fluid Mech.* **488**, 213–223.

Kistler, S. F. & Scriven, L. E. 1984 Coating flows. In *Computational Analysis of Polymer Processing* (ed. J. R. A. Pearson and S. M. Richardson), pp. 243–299. Applied Science.

Liberzon, D., Shemer, L. & Barnea, D. 2006 Upward-propagating capillary waves on the surface of short Taylor bubbles. *Phys. Fluids* **18**, 048103.

Mao, Z.-S. & Dukler, A. E. 1990 The motion of Taylor bubbles in vertical tubes I. A numerical simulation for the shape and rise velocity of Taylor bubbles in stagnant and flowing liquids *J. Comput. Phys.* **91**, 132–160.

Mao, Z.-S. & Dukler, A. E. 1991 The motion of Taylor bubbles in vertical tubes II. Experimental data and simulations for laminar and tubulent flow. *Chem. Engng Sci.* **46**, 2055–2064.

Moore, D. W. 1959 The rise of a gas bubble in a viscous liquid. *J. Fluid Mech.* **6**, 113–130.

Moore, D. W. 1965 The velocity of rise of distorted gas bubbles in a liquid of small viscosity. *J. Fluid Mech.* **23**, 749–766.

Mukundakrishnan, K., Quan, S., Eckmann, D. M. & Ayyaswamy, P. S. 2007 Numerical study of wall effects on buoyant gas-bubble rise in a liquid-filled finite cylinder. *Phys. Rev.* E **76**, 036308.

Nigmatulin, T.-R. & Bonetto, F. J. 1997 Shape of Taylor bubbles in vertical tubes. *Intl Commun. Heat Mass Transfer* **24**, 1177–1185.

Ortega, J. M. & Rheinoldt, W. C. 1970 *Iterative Solution of Nonlinear Equations in Several Variables.* Academic.

Reinelt, D. A. 1987 The penetration of a finger into a viscous fluid in a channel and tube. *J. Fluid Mech.* **175**, 557–565.

Ryskin, G. & Leal, L. G. 1984 Numerical solution of free-boundary problems in fluid mechanics. Part 2. Buoyancy-driven motion of a gas bubble through a quiescent liquid. *J. Fluid Mech.* **148**, 19–35.

de Santos, J. M. 1991 Two-phase cocurrent downflow through constricted passages. PhD thesis, University of Minnesota.

Strang, G. & Fix, G. J. 1973 *An Analysis of the Finite Element Method.* Prentice-Hall.

Taha, T. & Cui, Z. F. 2006 CFD modelling of slug flow in vertical tubes. *Chem. Engng Sci.* **61**, 676–687.

Taylor, T. D. & Acrivos, A. 1964 On the deformation and drag of a falling viscous drop at low Reynolds number. *J. Fluid Mech.* **18**, 166–176.

Tomiyama, A., Sou, A. & Sakaguichi, T. 1996 Numerical simulation of a Taylor bubbles in a stagnant liquid inside a vertical pipe. *JSME Intl J.* **B39**, 517–523.

Viana, F., Pardo, R., Yánez, R., Trallero, J. L. & Joseph, D. D. 2003 Universal correlation for the rise velocity of long gas bubbles in round pipes. *J. Fluid Mech.* **494**, 379–398.

Wallis, G. B. 1969 *One Dimensional Two-Phase Flow*. McGraw-Hill.

Wegener, P. P. & Parlange, J.-Y. 1973 Spherical-cap bubbles. *Annu. Rev. Fluid Mech.* **5**, 79–100.

White, E. T. & Beardmore, R.-H. 1962 The velocity of rise of single cylindrical air bubbles through liquids contained in vertical tubes. *Chem. Engng Sci.* **17**, 351–361.

Zukoski, E. E. 1966 Influence of viscosity, surface tension, and inclination angle on motion of long bubbles in closed tubes. *J. Fluid Mech.* **25**, 821–837.